

# A numerical study of swash flows generated by bores

Qinghai Zhang<sup>a</sup>, Philip L.-F. Liu<sup>a,b,\*</sup>

<sup>a</sup> School of Civil and Environmental Engineering, Cornell University, Ithaca, NY 14853, USA

<sup>b</sup> Institute of Hydrological and Oceanic Science, National Central University, Jhongli, Taiwan

## ARTICLE INFO

### Article history:

Received 10 October 2007

Received in revised form 15 March 2008

Accepted 4 April 2008

Available online 4 June 2008

### Keywords:

Swash zone

Tsunami runup

Dam-break

Bore

Non-linear shallow water equations

Reynolds averaged Navier–Stokes equation

Non-linear  $k-\epsilon$  model

## ABSTRACT

The dynamic processes of bore propagation over a uniform slope are studied numerically using a 2-D Reynolds Averaged Navier–Stokes (RANS) solver, coupled to a non-linear  $k-\epsilon$  turbulence closure and a volume of fluid (VOF) method. The dam-break mechanism is used to generate bores in a constant depth region. Present numerical results for the ensemble-averaged flow field are compared with existing experimental data as well as theoretical and numerical results based on non-linear shallow water (NSW) equations. Reasonable agreement between the present numerical solutions and experimental data is observed. Using the numerical results, small-scale bore behaviors and flow features, such as the bore collapse process near the still-water shoreline, the ‘mini-collapse’ during the runup phase and the ‘back-wash bore’ in the down-rush phase, are described. In the case of a strong bore, the evolution of the averaged turbulence kinetic energy (TKE) over the swash zone consists of two phases: in the region near the still-water shoreline, the production and the dissipation of TKE are roughly in balance; in the region farther landwards of the still-water shoreline, the TKE decay rate is very close to that of homogeneous grid turbulence. On the other hand, in the case of a weak bore, the bore collapse generated turbulence is confined near the bottom boundary layer and the TKE decays at a much slower rate.

© 2008 Elsevier B.V. All rights reserved.

## 1. Introduction

The swash zone is the part of beach face between the maximum runup and rundown of water waves, where the interaction between marine processes (e.g., wave breaking (Peregrine, 1983; Lin and Liu, 1998a,b)), and terrestrial processes (e.g., coastal ground-water table (Turner and Nielsen, 1997; Turner, 1998) and ground-water dynamics (Horn, 2006)) occurs. The hydrodynamics inside the swash zone is fundamental in understanding various phenomena including coastal erosion (Sallenger et al., 2002; Larson et al., 2004), wave–structure interaction (Peregrine and Williams, 2001; Liu and Al-Banaa, 2004), tsunami inundation (Liu et al., 2003, 2005), sediment transport and morphodynamics (Elfrink and Baldock, 2002; Baldock et al., 2005; Hsu and Raubenheimer, 2006; Masselink and Puleo, 2006).

In the early research, analytical approaches with simplifying assumptions (e.g., Whitham, 1958; Ho and Meyer, 1962; Shen and Meyer, 1963a,b) provided significant physical insights. Experimentally, quantitative data are difficult to obtain due to aeration, small thickness of the flow region, and complex dynamic nature of swash flows. This situation has been somewhat alleviated by the recent advancement of new measurement techniques such as laser Doppler velocimetry (LDV), particle imaging velocimetry (PIV) and ultrasonic sensors. Using these techniques, researchers have performed experiments in labora-

tory created swash zone (Petti and Longo, 2001; Cowen et al., 2003; Shin and Cox, 2006) as well as in field (Raubenheimer, 2002; Masselink and Russell, 2006; Baldock and Hughes, 2006).

The family of theoretical and numerical models for swash flows with the longest history is based on the NSW equations:

$$\frac{\partial \eta'}{\partial t'} + \frac{\partial}{\partial x'} [(\eta' + h')u'] = 0, \quad (1)$$

$$\frac{\partial u'}{\partial t'} + u' \frac{\partial u'}{\partial x'} + g \frac{\partial \eta'}{\partial x'} = 0. \quad (2)$$

where  $x'$  points horizontally in the landward direction,  $u'(x', t')$  is the depth-averaged water particle velocity,  $\eta'(x', t')$  the water surface elevation from the still-water level,  $h'(x')$  the water depth and  $g$  the gravitational acceleration.

A bore is defined theoretically as a moving discontinuity at  $x' = x'_b$  where  $u'$  jumps from 0 to  $u'(x'_b)$  and water surface elevation from  $h'(x'_b)$  to  $h'(x'_b) + \eta'(x'_b)$  (Stoker, 1957). The bore front velocity, defined as

$$U_f = \frac{dx'_b}{dt'} \quad (3)$$

can be calculated from Eqs. (1) and (2) as (Stoker, 1957):

$$U_f^2 = \frac{g(\eta' + h')(\eta' + 2h')}{2h'}. \quad (4)$$

Using the advancing and receding characteristic parameters as independent variables, Meyer and his colleagues studied shoaling of a

\* Corresponding author. School of Civil and Environmental Engineering, Cornell University, Ithaca, NY 14853, USA.

E-mail addresses: [qz27@cornell.edu](mailto:qz27@cornell.edu) (Q. Zhang), [pll3@cornell.edu](mailto:pll3@cornell.edu) (P.L.-F. Liu).

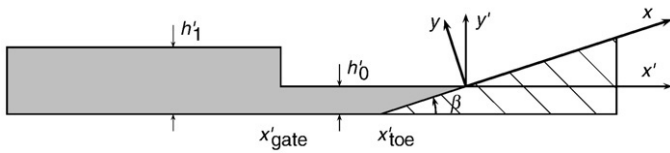


Fig. 1. The experimental and numerical setup of dam-break generated bores running up a slope.

bore (Ho and Meyer, 1962; Shen and Meyer, 1963b) and subsequent runup (Shen and Meyer, 1963a) on non-uniform slopes. They found that the behavior of a bore at the shoreline only depends on the local slope at the shoreline and the bore front velocity in the constant water depth region. In other words, different wave shapes and beach configurations along the bore path tend to be forgotten as the bore reaches the shoreline. As noted by Peregrine and Williams (2001), the solution given by Shen and Meyer (1963a) is only relevant when the shoreline is moved impulsively due to arrival of a bore. More recently, Baldock and his associates (Hughes and Baldock, 2004; Guard and Baldock, 2007) showed that the flow depth and velocity in the lower swash zone depend largely on the incident wave conditions at the seaward swash boundary.

Hibberd and Peregrine (1979) numerically solved Eqs. (1) and (2), using a finite difference method with the Lax and Wendroff (1960) scheme. Packwood (1980) extended this numerical model by incorporating the bottom friction effect with a Chezy term. However, the calculated runup heights are still much larger than those of the experimental results by Miller (1968), particularly in the cases of mild slopes.

Miller (1968) performed extensive experiments on bore runup on a uniform slope. He demonstrated that the bore does not collapse abruptly to zero at the still-water shoreline. Instead, there is a gradual

transition from the bore shoaling mode to the runup mode. Later experiments by Yeh and Ghazali (1988) further illustrated the interaction between the bore collapse and the water wedge in front of it. They observed and reported that the bore tends to push up the water wedge. This behavior is very different from the shallow water equation solutions.

Turbulence generation and dissipation due to wave breaking and bore collapse are important elements in swash flows. Madsen and Svendsen (1983) studied the quasi-steady bore propagation on a constant water depth with an algebraic  $k-\epsilon$  turbulence closure. The turbulence was assumed to be concentrated in a wedge that originates at the toe of the wave front and spreads towards the bottom. Their model provides information on the free surface profile, velocity and shear stress variations and dissipation within the bore. Svendsen and Madsen (1984) relaxed their previous assumption of quasi-steady state and investigated a turbulent bore evolution over varying water depth. While their model shed some lights on the turbulence field before the bore reaches the shoreline, it was not applicable to the bore collapse and the ensuing runup. Conceptually, most modeling efforts in coupling the turbulence models and the depth-averaged wave models are problematic in that the local processes such as the wave breaking that generate turbulence cannot be represented properly because the strong vertical velocity variation is not allowed in the depth-averaged wave models.

More recently, researchers have found that the acceleration of local fluid particles might be another important quantity for sediment transport in swash zone (Drake and Calantoni, 2001; Nielsen, 2002; Puleo, 2003). Using a RANS-based model, Puleo et al. (2007) investigated the temporal and spatial structure of accelerations for surging, plunging and nearly spilling waves. They found that accelerations have the largest magnitudes near the wave run down limit and are poorly correlated to near-bed pressure gradients.

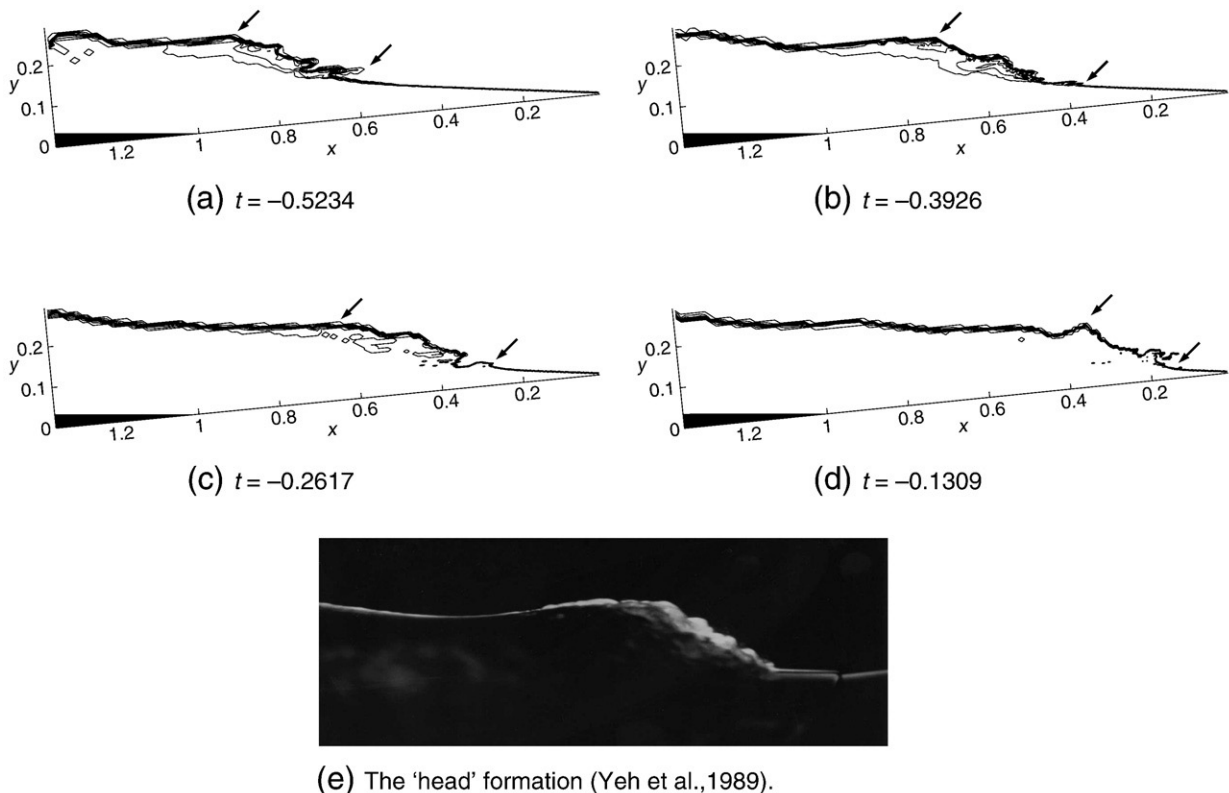


Fig. 2. Shoaling of the strong bore. Eight contour lines of the volume-fraction of water from 0 to 1 are plotted in (a)–(d), where the arrows indicate the locations of the bore head and bore toe. The formation of a bore 'head' is clearly shown in the photograph (e) and numerical results in (a) and (b).

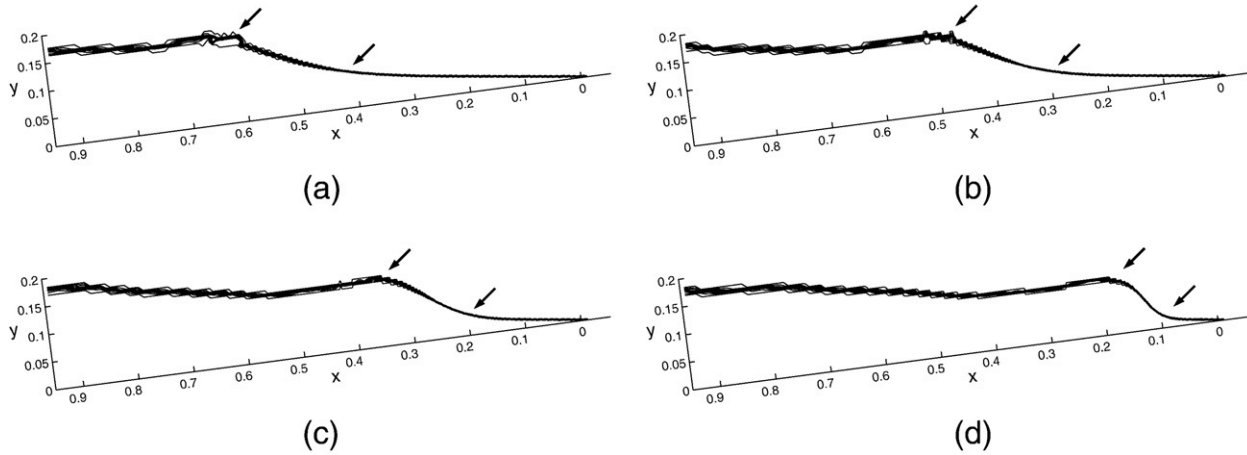


Fig. 3. Shoaling of the weak bore. See Fig. 2 for caption.

Based on the work of *Kothe and Mjolsness (1992)* and *Lemos (1992)*, *Lin and Liu (1998a)* presented a wave-breaking model called COBRAS. Although COBRAS was initially developed for the surf zone flows, it has been extended to many other applications, e.g., solitary wave runup (*Lin et al., 1999*), dam-break waves on a horizontal bed (*Shigematsu et al., 2004*), wave interactions with porous structures (*Liu et al., 1999; Hsu et al., 2002; Garcia et al., 2004; Lara et al., 2006*) and sediment transport in the surf and swash zone (*Hsu et al., 2003; Hsu and Liu, 2004; Amoudry et al., 2008*).

In this paper, we extend COBRAS to simulate dam-break generated bores, propagating, running up and running down over a sloping beach. The primary objective is to investigate the ensemble-averaged flow field and the TKE evolution during the shoaling, collapse, runup and down-rush processes. We shall demonstrate that the present numerical results for the ensemble-averaged flow field are in good agreement with existing experimental data (*Yeh and Ghazali, 1988; Yeh et al., 1989*). Moreover, the present numerical results also provide an opportunity to examine several small-scale flow features during the runup and down-rush phases.

In the next section, experimental and numerical setups for generating the dam-break bores are explained. In Section 3, we give a brief description of COBRAS, as well as initial and boundary conditions. In Section 4, we shall discuss the present numerical results with respect to different phases: shoaling, collapse, runup and down-rush. Numerical results are compared with previous experimental data and theoretical results based on the NSW equations. The ensemble-averaged velocity fields as well as the TKE evolution are discussed. Small-scale features such as the ‘mini-collapse’ during the

runup phase and the ‘back-wash bore’ in the down-rush phase are investigated. Some concluding remarks on the turbulence modeling are given in the last section.

2. Setup

*Yeh and Ghazali (1988)* and *Yeh et al. (1989)* studied experimentally bore collapse and runup over a uniform slope. Their bores were generated by a dam-break mechanism in a flume, as sketched in Fig. 1. The water depth in front of the dam (gate) was  $h'_0$  and the water depth behind it  $h'_1$ . The gate at  $x'_{gate} = 12 h'_0$  was pulled instantaneously and the resulting bore ran up a slope of  $\beta = 7.5^\circ$ . To characterize this experimental setup, we choose the length-scale, the velocity-scale and the time-scale as

$$L_* = \frac{h'_0}{\sin \beta}, \quad U_* = \sqrt{gh'_0}, \quad T_* = \frac{L_*}{U_*}. \tag{5}$$

In this paper, the numerical setup is the same as the experimental setup, except that the coordinates of the numerical model are rotated so that the  $x$ -axis coincides with the slope face. The spatial and temporal coordinates are also non-dimensionalized by  $L_*$  and  $T_*$ , respectively:

$$x = \frac{x' \cos \beta + y' \sin \beta}{L_*}, \quad y = \frac{-x' \sin \beta + y' \cos \beta}{L_*}, \quad t = \frac{t'}{T_*}. \tag{6}$$

The toe of the slope is then at  $x_{toe} = -1$  and  $t = 0$  corresponds to the instant when the still-water shoreline at  $x = 0$  starts to move landward due to an incoming bore.

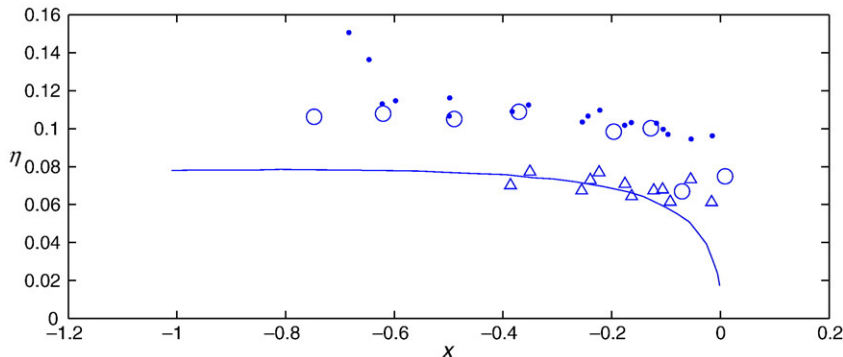


Fig. 4. The bore height evolution in the shoaling phase. — (strong bore) represents theoretical results of *Ho and Meyer (1962)*; ● (strong bore,  $\eta$  is based on the bore head) and  $\Delta$  (strong bore,  $\eta$  is behind the bore head) denote experimental data of *Yeh et al. (1989)*; ○ (strong bore,  $\eta$  is based on bore head) represents present numerical results.

The arrangement of  $x$ - $y$  axes allows us to remove a crucial numerical difficulty: the partial cell (non-boundary-conforming cell) treatment. In the original COBRAS (Lin and Liu, 1998a) and its applications to solitary waves over sloping beaches (Lin et al., 1999), a solid obstacle inside the computational domain is treated as a special case of a flow with an infinite density. The cell area is partially blocked according to boundary geometry of the solid obstacle; an openness coefficient  $\theta$  is defined as the ratio of the volume not occupied by the obstacle to the total cell volume. Thus  $\theta=0$  if the cell is entirely occupied by the obstacle;  $\theta=1$  if the cell is entirely occupied by fluid; and  $0<\theta<1$ , if the cell is partially occupied by the obstacle. All physical variables in the partial cells or on the cell faces are modified as the product of the original value of the physical variables by the openness coefficient  $\theta$ . Near the obstacle, the openness coefficients makes the

modified quantities smaller than their original values. In this way, the effect of obstacle is incorporated into all the governing equations and hence no boundary conditions need to be specified at the irregular obstacle boundaries inside the computational domain.

Although this type of partial cell treatment is convenient to implement, it has several shortcomings, particularly in the swash zone case. Firstly, since velocity and pressure of a partial cell are scaled by the openness coefficient  $\theta$ , gravity must also be scaled by  $\theta$  in order to close the RANS equations. This modification to gravity ( $\theta g$ ) is strictly speaking not correct. Secondly, the pressure calculation is strongly coupled to the location of the grids. Thirdly, the directional information of a solid–fluid interface is not defined accurately by the scalar  $\theta$ . Lastly and most importantly, the boundary conditions of all physical variables are modified by this treatment. Consequently,

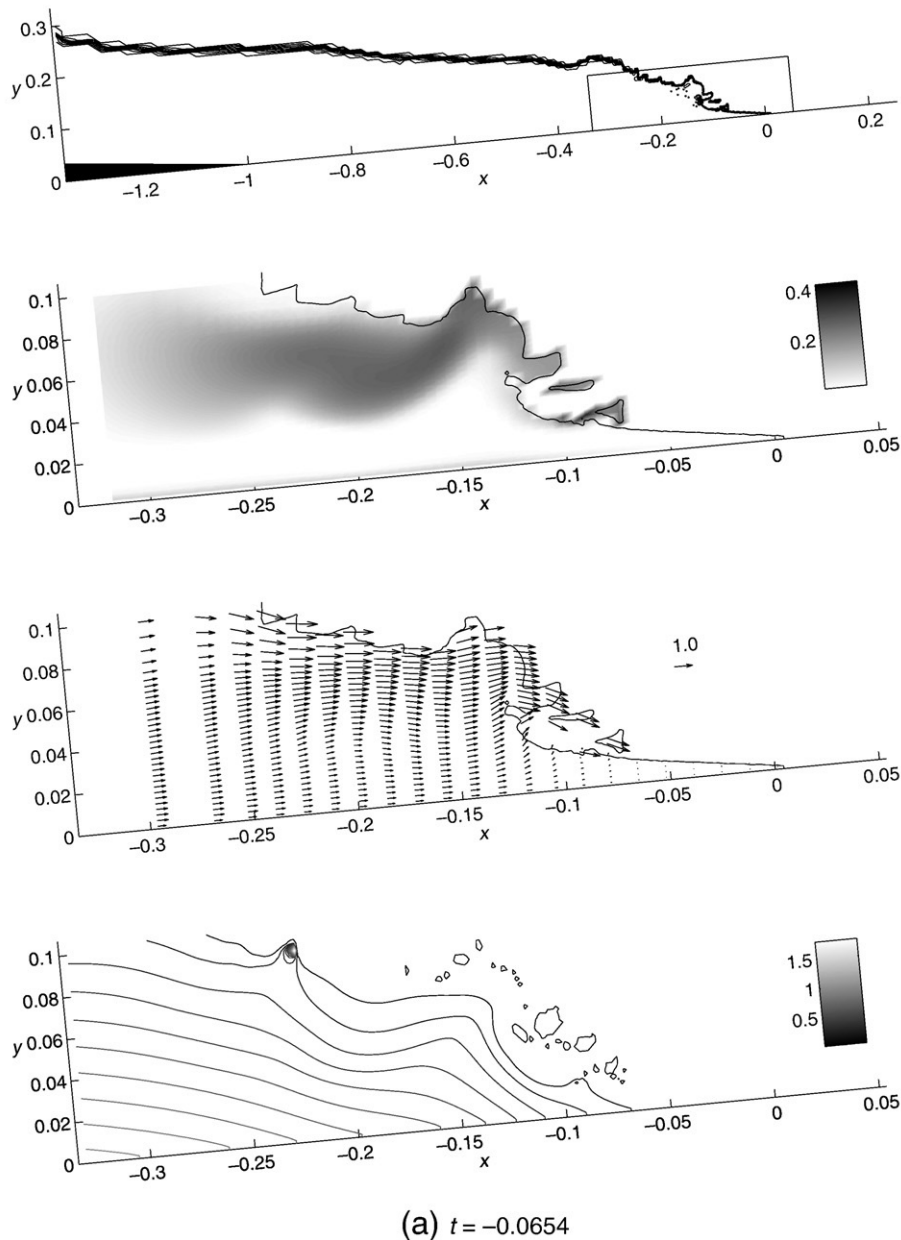


Fig. 5. Collapse of the strong bore. Four subplots are shown for each of the four snapshots. Eight contour lines of the volume-fraction of water from 0 to 1 are plotted in the first subplot to show an overview of the free surface profile. The other three subplots are zoom-ins of a small-window in the first subplot. The gray-map of  $\sqrt{k}$  is shown in the second subplot and dimensionless velocity and pressure fields are plotted in the third and fourth subplot.

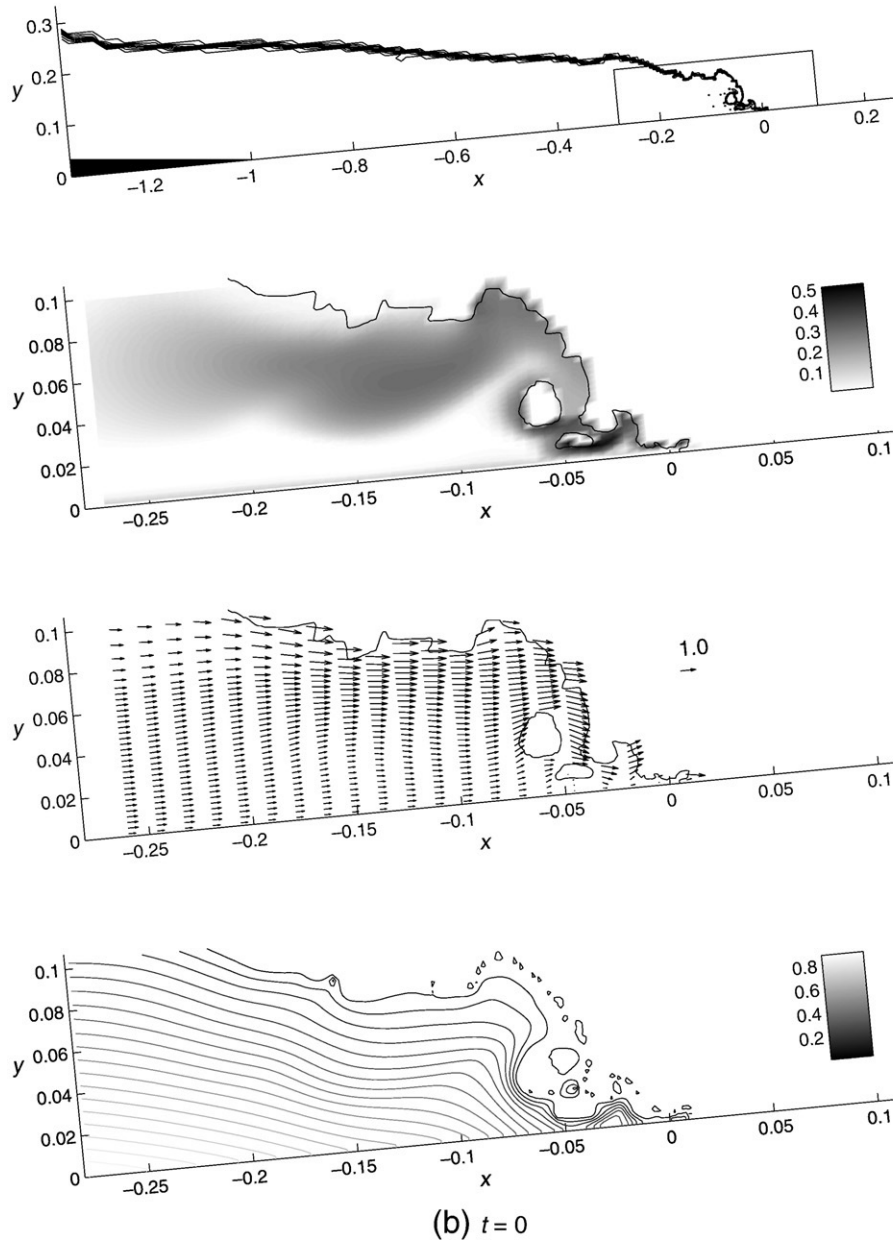


Fig. 5 (continued).

the wall effect upon the ensemble-averaged velocity field and the turbulence field is not adequately simulated near a solid obstacle. This treatment is acceptable if we are only interested in flow region far away from partial cells. However, for the swash zone simulations, the errors created by the partial cell treatment will strongly affect the solutions because the water depth is very small.

Fortunately, if we simply rotate the coordinates to align the abscissa with the slope face, the need for a partial cell treatment in the swash zone is eliminated for the uniform beach cases. This facilitates the accurate application of boundary conditions along the beach face. Although partial cells in the flat-bed region are unavoidable, their effects are confined in a relatively unimportant and uninteresting region for the present study.

In reality, the beach configuration is complex. The simple approach used herein will not work. Other numerical algorithms, such as the Immersed Boundary Method (Peskin, 1972, 1977) or the Immersed

Interface Method (Leveque and Li, 1994; Li and Lai, 2001), among many other options, should be used. We will not pursue this issue in this paper so that we can focus on the physical processes in swash flows.

### 3. Implementation

#### 3.1. Numerical models

In the rotated  $x$ - $y$  coordinates, the ensemble-averaged velocity field is governed by the following non-dimensional RANS equations:

$$\frac{\partial \langle U_i \rangle}{\partial x_i} = 0 \tag{7}$$

$$\frac{\partial \langle U_i \rangle}{\partial t} + \langle U_j \rangle \frac{\partial \langle U_i \rangle}{\partial x_j} = -\frac{\partial \langle p \rangle}{\partial x_i} + g_i + \frac{1}{Re} \frac{\partial^2 \langle U_i \rangle}{\partial x_j \partial x_j} - \frac{\partial \langle u_i u_j \rangle}{\partial x_j} \tag{8}$$

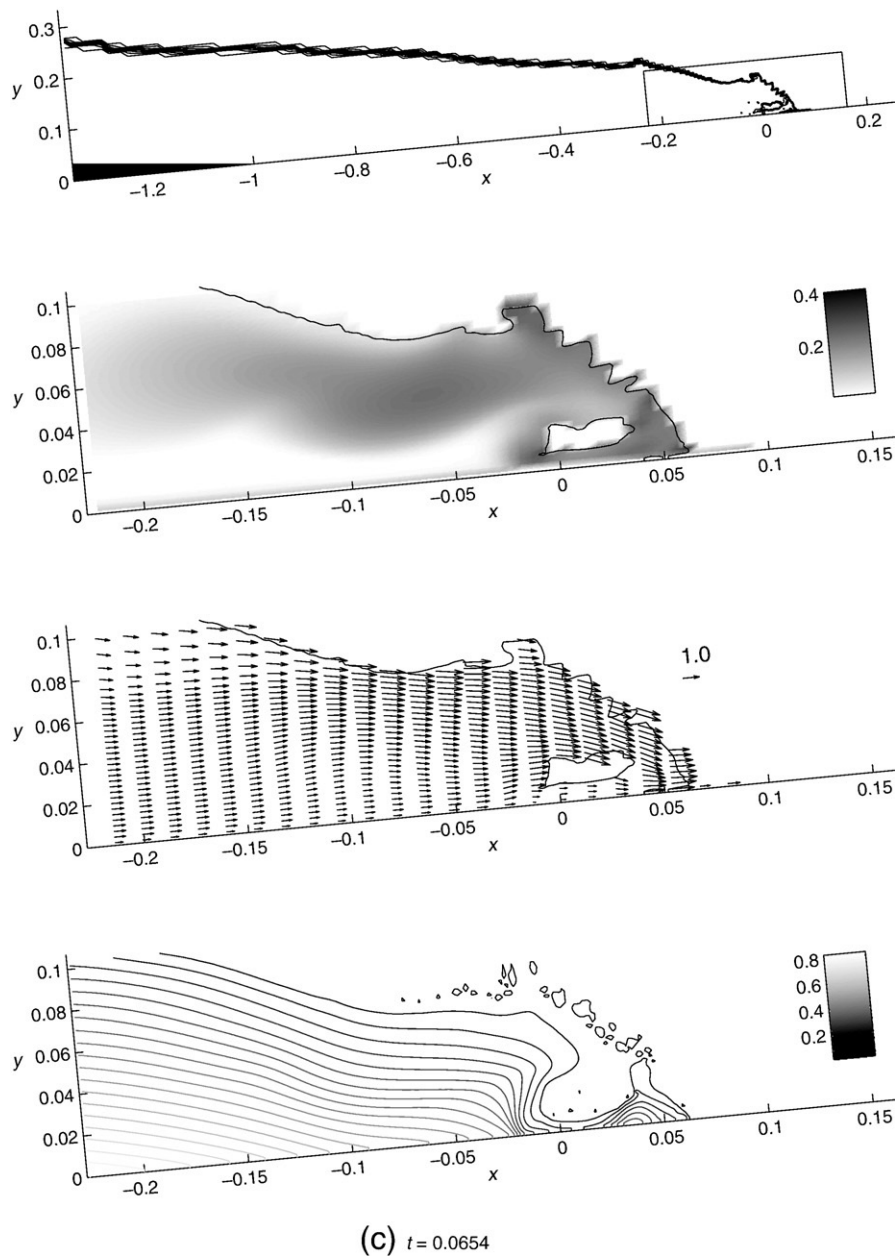


Fig. 5 (continued).

where  $U_j$  is the  $j$ -th component of the total velocity (normalized by  $U_*$ ),  $\langle \cdot \rangle$  denotes the ensemble average operator and  $u_j$  the corresponding fluctuating velocity component, thus  $U_j = \langle U_j \rangle + u_j$ . In the momentum equation (8),  $p$  is the total dynamic pressure and  $g_i$  the normalized gravity  $g_i = (g_x, g_y) = (1, 1 / \tan \beta)$ . The swash flows considered in this paper are turbulent due to the high Reynolds number

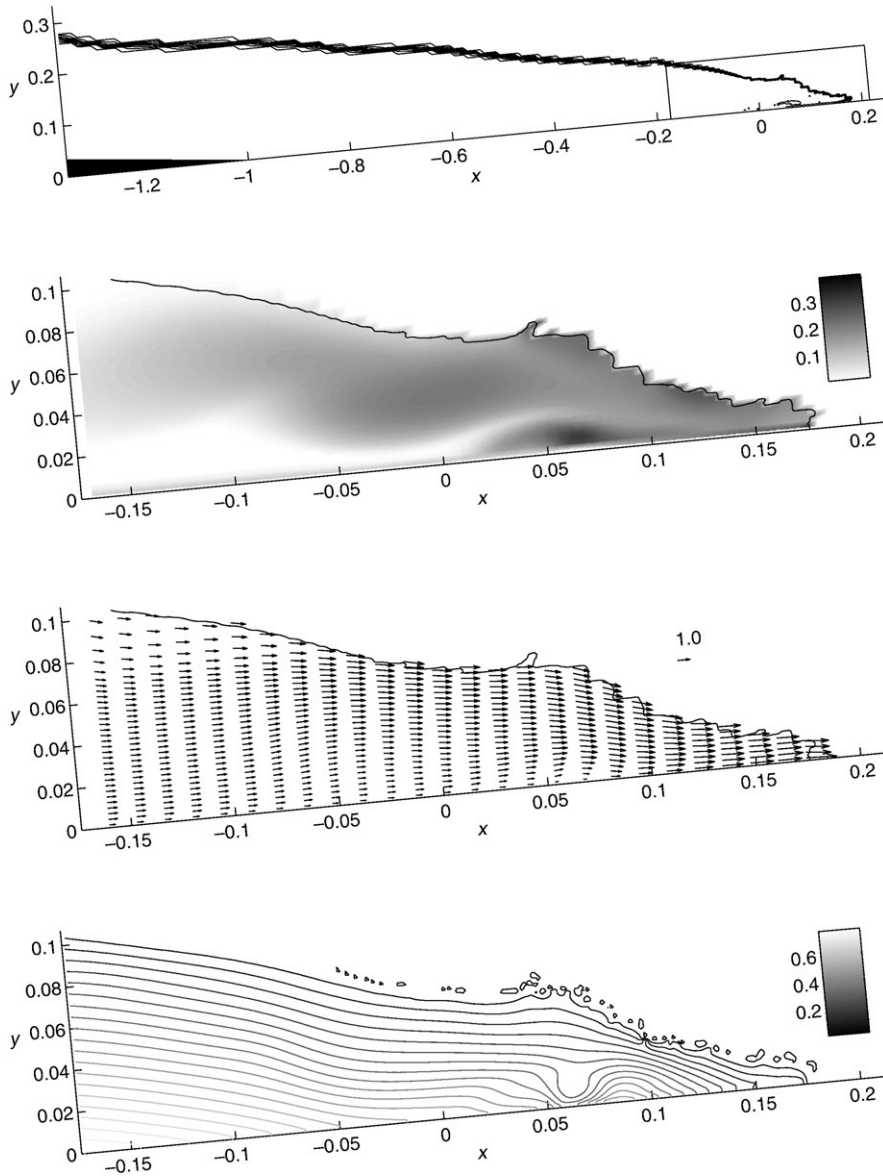
$$Re = \frac{U_* L_*}{\nu} = \frac{h'_0 \sqrt{gh'_0}}{\nu \sin \beta} = 7.30 \times 10^5, \tag{9}$$

where  $\nu$  is the kinematic viscosity of water.

The two-step projection method by Chorin (1968, 1969) is used to solve Eqs. (7) and (8). The first step introduces an inter-

mediate velocity field that results from forward-in-time explicit calculation of Eq. (8), without considering the pressure terms; the second step projects the intermediate velocity field onto a divergence free plane of Eq. (7) to obtain the velocity for the next time step.

A VOF method is used to track the surface by an advection step and a reconstruction step. New volume-fraction values are first calculated from previous values and interface configuration. Then the new interface is reconstructed from the new volume-fraction field. In this paper, we follow the SOLA–VOF method proposed by Hirt and Nichols (1981). This method represents the interface within each cell as either a vertical or a horizontal surface, the direction of which only depends on the spatial gradient of volume-fraction.



(d)  $t = 0.1309$

Fig. 5 (continued).

The turbulence field is studied by the  $k-\epsilon$  model (Jones and Launder, 1972):

$$\frac{\partial k}{\partial t} + \langle U_j \rangle \frac{\partial k}{\partial x_j} = \frac{\partial}{\partial x_j} \left[ \left( \frac{1}{\sigma_k Re_t} + \frac{1}{Re} \right) \frac{\partial k}{\partial x_j} \right] + \mathcal{P} - \epsilon, \quad (10)$$

$$\frac{\partial \epsilon}{\partial t} + \langle U_j \rangle \frac{\partial \epsilon}{\partial x_j} = \frac{\partial}{\partial x_j} \left[ \left( \frac{1}{\sigma_\epsilon Re_t} + \frac{1}{Re} \right) \frac{\partial \epsilon}{\partial x_j} \right] + C_{e1} \mathcal{P} \frac{\epsilon}{k} - C_{e2} \frac{\epsilon^2}{k}, \quad (11)$$

where  $Re_t = U_* L_* / \nu_t$  with  $\nu_t$  as the turbulent viscosity,  $k$  is the TKE (normalized by  $U_*^2$ ),  $\epsilon$  the rate of TKE dissipation (normalized by  $U_*^3 / T_*$ ) and  $\mathcal{P} = -\langle u_i u_j \rangle \frac{\partial \langle U_j \rangle}{\partial x_i}$  the TKE production (normalized by  $U_*^2 / T_*$ ). While the  $k$  equation can be viewed as exact with the turbulent flux terms modeled by gradient diffusion hypothesis, the  $\epsilon$  equation is

purely empirical. The constant coefficients in Eqs. (10) and (11), due to Launder and Sharma (1974),

$$C_{e1} = 1.44, \quad C_{e2} = 1.92, \quad \sigma_k = 1.0, \quad \sigma_\epsilon = 1.3, \quad (12)$$

are used in this work, since Rodi (1980) showed that the values of the coefficients in Eq. (12) are surprisingly universal.

For the specific assumption of turbulent viscosity hypothesis, we use the non-linear algebraic closure by Shih et al. (1996):

$$\begin{aligned} \langle u_i u_j \rangle = & \frac{2}{3} k \delta_{ij} - C_{\mu} \frac{k}{\epsilon} \left( \frac{\partial \langle U_i \rangle}{\partial x_j} + \frac{\partial \langle U_j \rangle}{\partial x_i} \right) \\ & - \frac{k^3}{\epsilon^2} C_1 \left( \frac{\partial \langle U_i \rangle}{\partial x_l} \frac{\partial \langle U_l \rangle}{\partial x_i} + \frac{\partial \langle U_j \rangle}{\partial x_l} \frac{\partial \langle U_l \rangle}{\partial x_j} - \frac{2}{3} \frac{\partial \langle U_i \rangle}{\partial x_k} \frac{\partial \langle U_k \rangle}{\partial x_l} \delta_{ij} \right) \\ & - \frac{k^3}{\epsilon^2} C_2 \left( \frac{\partial \langle U_i \rangle}{\partial x_k} \frac{\partial \langle U_j \rangle}{\partial x_k} - \frac{1}{3} \frac{\partial \langle U_l \rangle}{\partial x_k} \frac{\partial \langle U_l \rangle}{\partial x_k} \delta_{ij} \right) \\ & - \frac{k^3}{\epsilon^2} C_3 \left( \frac{\partial \langle U_k \rangle}{\partial x_i} \frac{\partial \langle U_k \rangle}{\partial x_j} - \frac{1}{3} \frac{\partial \langle U_l \rangle}{\partial x_k} \frac{\partial \langle U_l \rangle}{\partial x_k} \delta_{ij} \right). \end{aligned} \quad (13)$$

The empirical coefficients in Eq. (13) are given as follows,

$$\begin{cases} C_{\mu} = \frac{2}{3} \left( \frac{1}{7.4 + S_{\max}} \right), & C_1 = \frac{1}{185.2 + D_{\max}^2} \\ C_2 = \frac{1}{58.5 + D_{\max}^2}, & C_3 = \frac{1}{370.4 + D_{\max}^2} \end{cases} \quad (14)$$

where  $S_{\max} = \frac{k}{\epsilon} \max_i \left| \frac{\partial \langle U_i \rangle}{\partial x_i} \right|$  (indices not summed) and  $D_{\max} = \frac{k}{\epsilon} \max_i \left| \frac{\partial \langle U_i \rangle}{\partial x_i} \right|$ . The determination of Eq. (14) concerns a realization condition and recovering the non-linear closure to a linear one, the reader are referred to (Lin and Liu, 1998a) for a detailed discussion.

### 3.2. Spatial and temporal grids

Structured, non-uniform rectangular grids are used for computational efficiency and economy. The solutions presented herein use the grid resolution as follows: near and on the beach face the grid sizes are 1 mm × 1 mm and far away from the beach face grid sizes are about 10 times coarser; the grid size in the transitional region changes slowly ( $\Delta x_i / \Delta x_{i+1} < 1.05$ ) to ensure numerical stability. The convergence tests were conducted by using grid sizes of 2 mm × 2 mm and 0.5 mm × 0.5 mm. In spite of the very fine resolution, an estimation by the

continuum surface force (CSF) model (Brackbill et al., 1992) shows that the surface tension effect is still negligible in this application.

The choice of square grids in the wash zone is due to the VOF method (Hirt and Nichols, 1981) employed in COBRAS, which relies heavily on the gradient of the volume-of-fraction ( $\nabla F$ ) to determine the free surface orientation. Previous simulations show that a large ratio of spatial intervals ( $\Delta x / \Delta y$ ) often causes inaccurate free surface orientations. Here we simply adopt the square grids to prevent spurious results of interface reconstruction.

The size of time steps is dynamically adjusted to satisfy both advection and diffusion stability requirements:

$$\Delta t \leq \min \left( \frac{\alpha \Delta x}{\langle U \rangle_{\max}}, \frac{\alpha \Delta y}{\langle V \rangle_{\max}} \right) \quad (15)$$

$$\Delta t \leq \frac{1}{2(v_t + \nu)} \left[ \frac{\Delta x^2 \Delta y^2}{\Delta x^2 + \Delta y^2} \right] \frac{L_*^2}{T_*} \quad (16)$$

where  $\alpha = 0.3$  and  $\langle U \rangle_{\max}, \langle V \rangle_{\max}$  are the maximum dimensionless horizontal and vertical ensemble-averaged velocity in the computational domain.

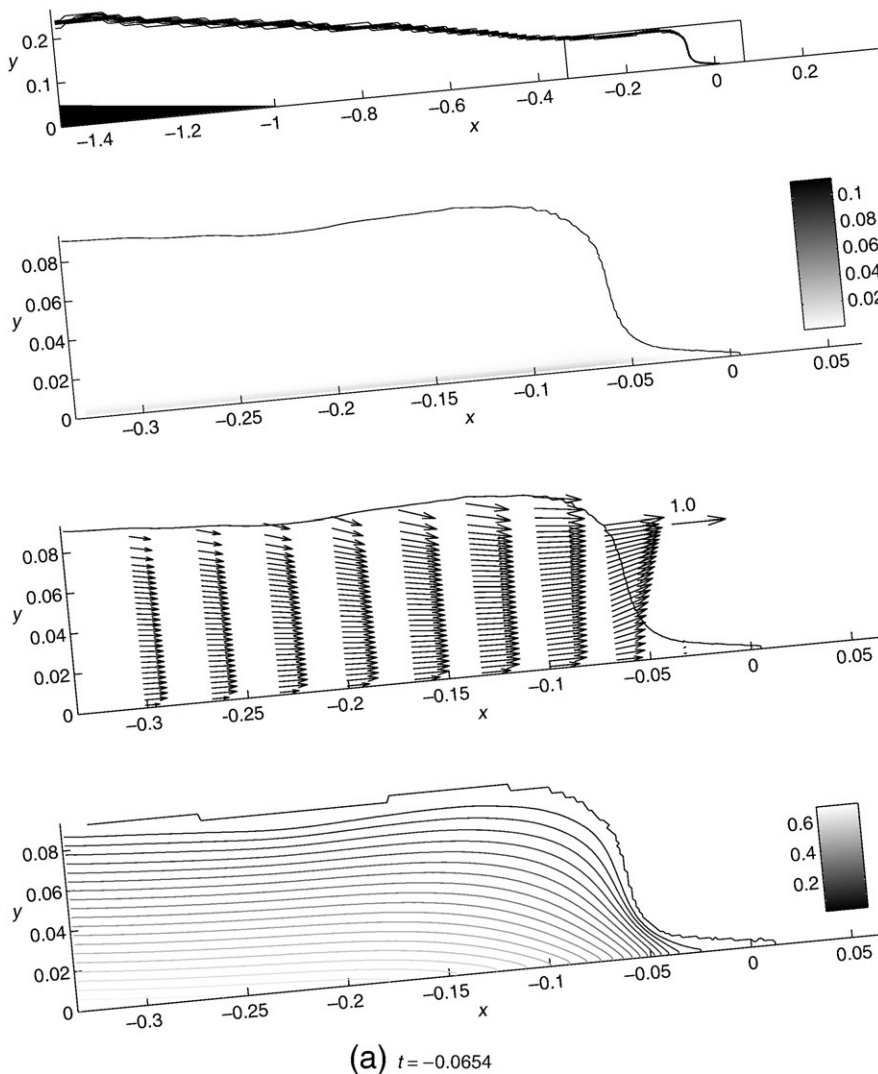


Fig. 6. Collapse of the weak bore. See Fig. 5 for caption.

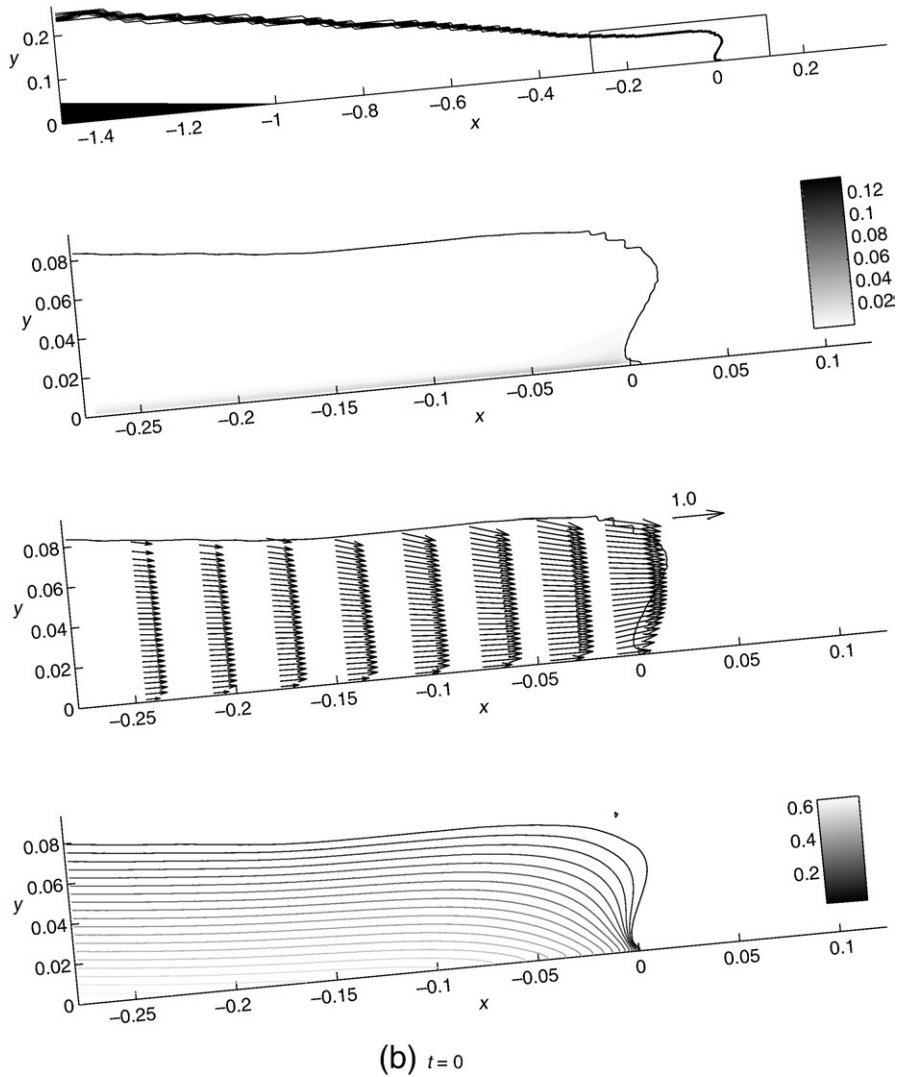


Fig. 6 (continued).

### 3.3. Initial and boundary conditions

The initial velocity is zero everywhere and the initial pressure is hydrostatic so that the numerical simulations mimic the experimental setup. As for the  $k-\epsilon$  model, it will not produce any TKE if there is no TKE initially. Thus, a small amount of  $k=(\delta c_0)^2/2$ , serving as ‘seed’, is specified everywhere at the initial time of computation, where  $\delta=2.5 \times 10^{-3}$  and  $c_0 = \sqrt{h_1/h_0}$ . In the strong bore case, the maximal value of  $k$  stays very low ( $O(10^{-6})$ ) until the generated bore reaches  $x=0$ , where  $k$  increased rapidly to a very high level ( $O(10^0)$ ). This implies that wave breaking at the initial-water shoreline ‘erases’ the initial memory of the turbulence field. Thus, initial seedings with  $\delta$  smaller than  $2.5 \times 10^{-3}$  essentially make no difference to our numerical results. This is also confirmed by Lin (1998).

The air phase is treated as void, i.e., the velocity and pressure in the air phase is set to zero at the beginning of every time step. This is an approximation to the zero stress conditions. The free surface is also treated as a flux barrier for turbulence field, i.e.,  $\partial k/\partial n=0$ ,  $\partial \epsilon/\partial n=0$ , where  $n$  is the local outward-normal direction of the free surface.

Along the solid wall, we impose no-slip boundary condition for the ensemble-averaged velocity. As for the turbulence field, a shear

velocity,  $u_\tau$ , is first calculated from the law of wall with the logarithmic velocity profile and it is then used as the velocity scale to calculate TKE and dissipation near the wall, i.e.:

$$\frac{\langle U_w \rangle}{u_\tau} = \frac{1}{\kappa} \ln \left( E \frac{u_\tau y_w}{\nu} \right), \quad (17)$$

$$k_w = \frac{u_\tau^2}{\sqrt{C_\mu}}, \quad \epsilon_w = \frac{u_\tau^3}{\kappa y_w}, \quad (18)$$

where subscript  $w$  denotes a dimensional quantity evaluated at one grid away from the wall. For a smooth wall,  $E=9.0$ ,  $\kappa=0.41$ , and  $C_\mu=0.09$  near the wall. In the strong bore collapse case, the shear velocity  $u_\tau \sim O(10^{-1})$ (m/s) and the viscous length scale near the wall is  $\delta_w = \nu/u_\tau \sim O(10^{-5})$ (m). The thickness of the viscous sub-layer is thus about 0.1 mm, which is roughly one order of magnitude smaller than our grid size. This confirms the validity of the log-law boundary conditions.

Before studying a bore running up the slope, it is important to make sure that the numerical model can generate the bore correctly through the dam-break mechanism. The verification of the numerical

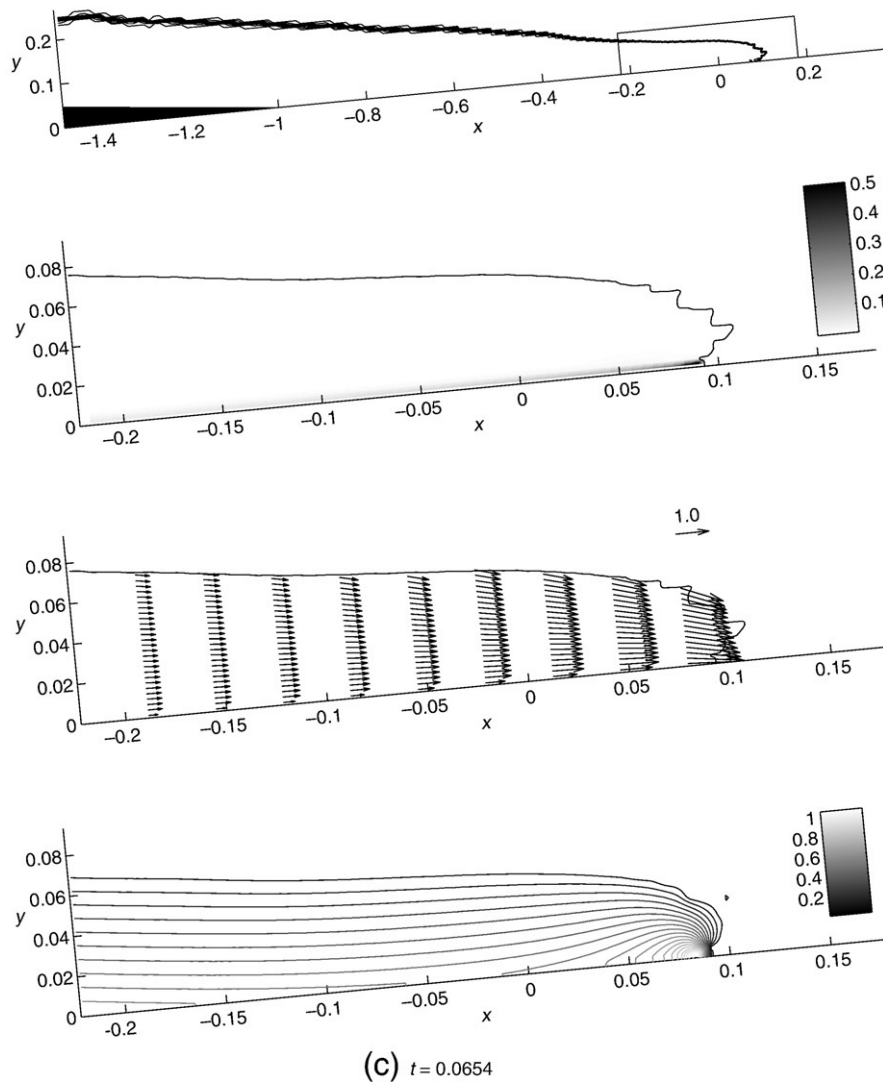


Fig. 6 (continued).

model for the bore generation on a flat bed has been shown in our previous work (Shigematsu et al., 2004) and will not be repeated here.

#### 4. Results

In the experiments by Yeh et al. (1989), different values of  $h_1/h_0$  were used. A relevant Froude number (Sturtevant, 1965)

$$F_r = \frac{U_f}{\sqrt{gh_0}} \quad (19)$$

measures the strength of a bore, where  $U_f$  is defined in Eq. (4). For the strong bore  $h_0=9.75$  cm and  $h_1=22.52$  cm yields  $F_r=1.43$  and  $h_1/h_0=2.31$ , for the weak bore  $h_0=9.75$  cm and  $h_1=16.72$  cm corresponds to  $F_r=1.18$  and  $h_1/h_0=1.72$ . We note that Yeh et al. (1989) called the former case as a fully developed turbulent bore (FDTB) and the latter a undular bore (UB).

The physical process of a bore propagating up a slope can be divided into four phases: shoaling, collapse, runup and down-rush.

We shall present the numerical results according to the sequence of these events.

##### 4.1. Shoaling

Four snapshots of free surface profiles are plotted in Fig. 2 to show the shoaling of the strong bore and in Fig. 3 for the weak bore. In each panel, eight contour lines of  $F$ -values (volume-fraction of water) from 0 to 1 (0 denotes an air-cell and 1 a water-cell) are shown. The relative wide spreading of these contour lines in Fig. 2 implies that the mixing of water and air, i.e., breaking, is strong in the front face of the strong bore, while the closeness of these contour lines in Fig. 3 suggests no wave breaking in the case of the weak bore. Yeh et al. (1989) reported that the free surface profile of the strong bore forms a distinct 'head' at the front and the total water depth behind the head is noticeably smaller, as shown in Fig. 2(e). The present numerical results simulate this feature very well, as displayed in Fig. 2(b). Following Yeh et al. (1989), we define the 'bore head position' as the location where the maximum water depth occurs within the bore front and the 'bore position' as the position of the bore toe, as marked by the arrows in

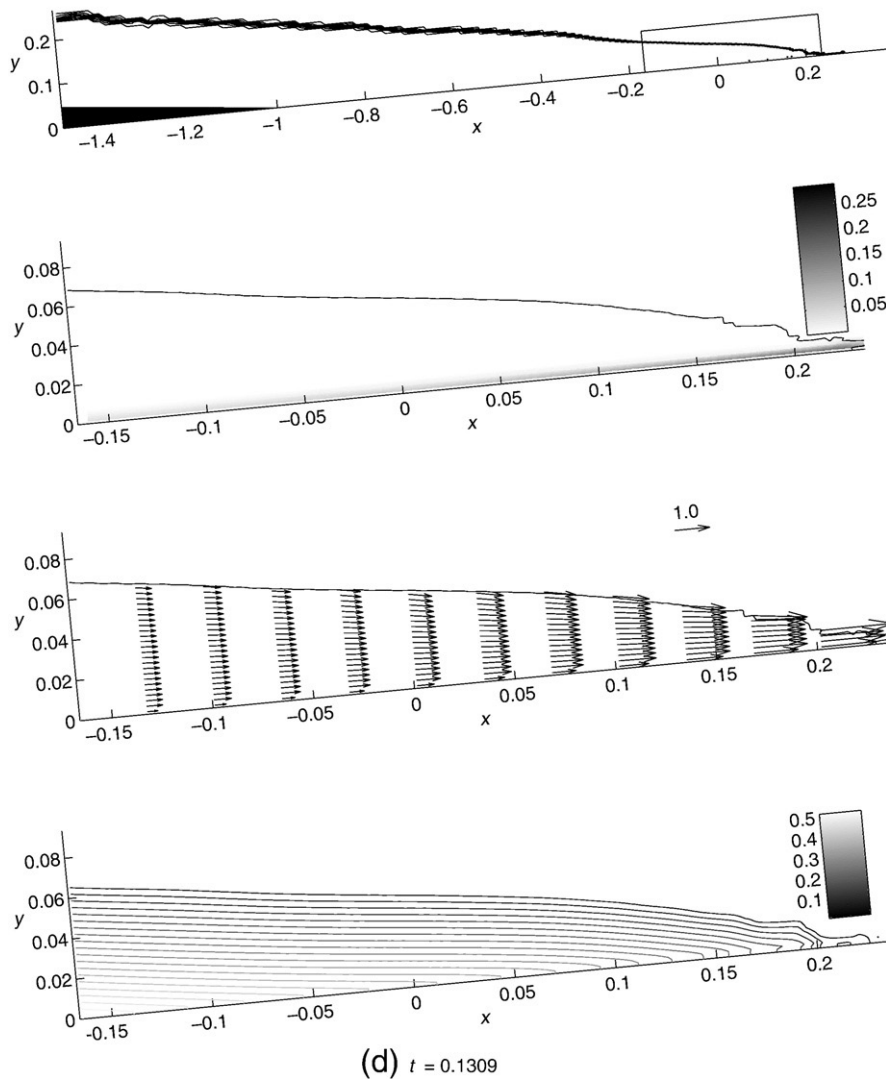


Fig. 6 (continued).

Figs. 2 and 3. Numerically, the bore toe is determined by locating the most landward position where the increase of the water depth is larger than  $2\Delta y$  in 20 computational time steps.

The evolution of bore heights ( $\eta = \eta' \cos \beta / L^*$ ) for the strong bore during the shoaling phase is plotted in Fig. 4. The bore height can be defined as the water depth at either the bore head or the shallower depth behind the bore head (see Fig. 2(e)). Experimental data deviates from constant depth for  $x < -0.6$ . This might be caused by imperfection of the experiments, as noted by Yeh et al. (1989). It is interesting to observe that the theoretical NSW results (Ho and Meyer, 1962) agree with the bore height measured behind the bore head quite well away from the still-water shoreline. The NSW theory predicts that the bore height diminishes to zero at the still-water shoreline. However, experimental data and the present numerical results show that the bore heights remain constant over most of the shoaling phase. In reality the bore front becomes much more aerated when it breaks near  $x=0$ . However, COBRAS treats the surface as sharp and is thus incapable of modeling the detailed evolution of the air–water mixture. Also, we do not consider trapped air bubbles when extracting the bore height information from the volume-fraction results. These might be the reasons that the bore heights of

our numerical results fall noticeably below the experimental results near the still-water shoreline.

#### 4.2. Collapse

During the bore collapse phase, the bore front collapses onto the slope and loses its steep free surface profile. Four snap shots of the bore collapse process, in terms of free surface profile, ensemble averaged velocity and TKE, for the strong bore are shown in Fig. 5 and for the weak bore in Fig. 6.

In the strong bore case, the bore breaks during the shoaling and before arriving at the still-water shoreline. As shown in Figs. 2 and 5 (a), climbing the slope further steepens the bore front and fluid particles near the bore head travel faster than those near the beach face. Large vertical gradients of the velocity are clearly seen. Thus, the strong bore starts to collapse before it reaches the still-water shoreline, as shown in Fig. 5(b) and (c). As a result, a small still-water wedge in front of the collapsing bore is pushed up (Fig. 5(b)) and at the same time the bore is slowed down. This wedge of fluid serves as a ‘buffer’ between the bore and the slope and consequently, the bore collapse becomes less abrupt, although it still occurs in a relatively short time.

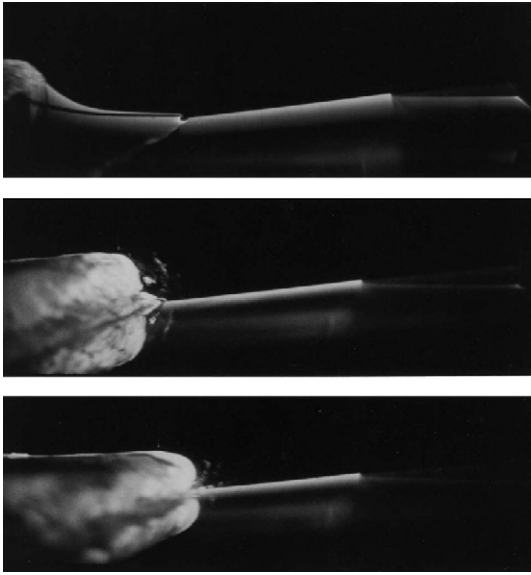


Fig. 7. Three photographs of the free surface profile during the collapse of a weak bore (Yeh et al., 1989).

These features confirm the experimental observations by Miller (1968) and Yeh and Ghazali (1988).

The bore collapse process in the weak bore case is different. Initially, the weak bore does not break during the shoaling phase (see Fig. 3). Fig. 6(a), (b) and (c) shows that the bore front transforms into a shape of letter 'D' close to the still-water shoreline. The gravity force pulls the bore front onto the beach face and thus the bore collapses. Experimental results of Yeh et al. (1989) illustrating these features are shown in Fig. 7. The PIV measurements of Jensen et al. (2003) also

demonstrated this 'D'-shape front for non-breaking solitary waves on a steeper slope.

Behind the bore head, the ensemble-averaged velocity is uniform in the water column for the weak bore case. In both bores, significant vertical (downward) velocity components are apparent near the end of the bore collapse as shown in Figs. 5(c) and 6(c). After the bore front loses its vertical profile, a water tongue is formed and is ready to run up the slope (Figs. 5(d) and 6(d)).

As for the turbulence field, the collapse of the weak bore generates relatively little turbulence, except near the bottom boundary layer at the end of the bore collapse process (see the second subplots of Fig. 6). It is very different in the strong bore case. Before the strong bore reaches the still-water shoreline, its frontal zone already contains highly concentrated turbulence, as shown in Fig. 5(a). During the bore collapse shown in Fig. 5(b) and (c), more turbulence is generated in the bore front and near the bottom boundary layer. At the end of the collapse phase, the turbulence is spread to a larger region as shown in Fig. 5(d).

In the strong bore case, the present numerical results show that a large air bubble was trapped inside the collapsing water (an air tube is formed in the span-wise direction in Fig. 5(c)). In the field condition, the bore collapse is three-dimensional and an air tube can be easily broken. Thus this detail of trapped air bubble should not be taken seriously. We also remark here that the effects of surface tension are not considered in the current model. As noted in Section 4.1, bore heights near the breaking sites have noticeable errors, since air bubbles are not considered when extracting bore height information from volume-fraction results. However, we argue that the dominant process in bore collapse is the momentum exchange of breaking surface and relatively insignificant are the surface tension effect and the detailed evolution of the air/water mixture. Furthermore, the air bubbles should not affect the ensuing runup because the related time scale is very small.

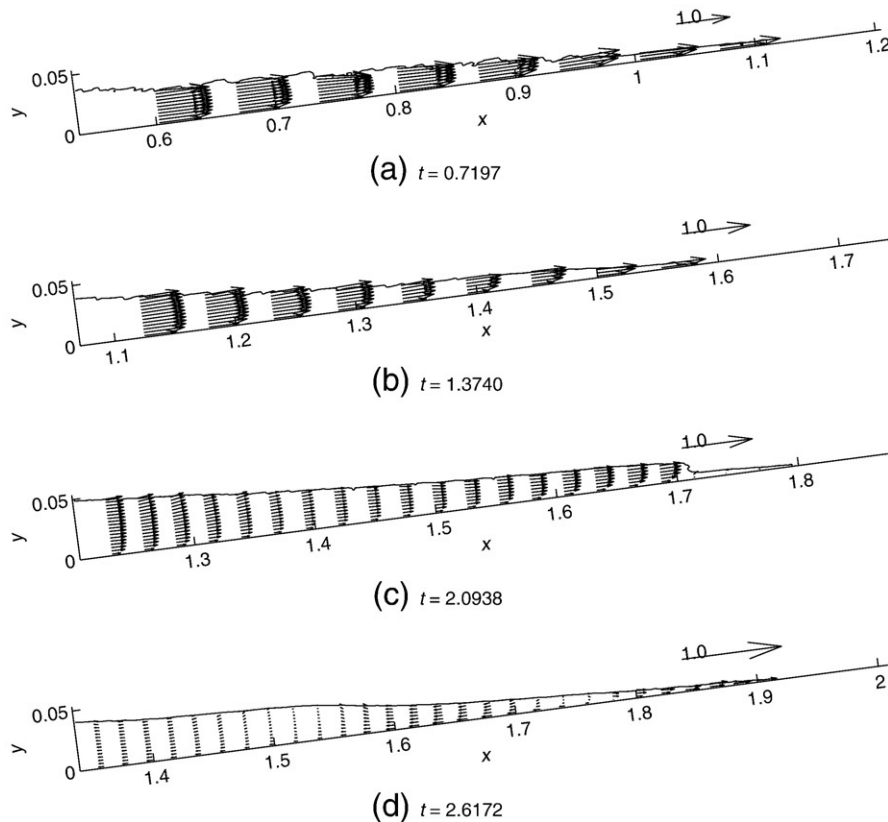


Fig. 8. Runup of the strong bore: non-dimensional mean velocity field ( $U$ ).

The pressure fields during the bore collapse phase are shown in the fourth subplots of Fig. 5 for the strong bore case and in Fig. 6 for the weak bore case. The hydrostatic pressure assumption appears to be reasonable in the regions away from the bore front and a short period after the collapse phase. It is also noted that large pressure gradients along the  $x$ -axis are present, which serve to accelerate the collapsing bore.

### 4.3. Runup

#### 4.3.1. Mean velocity field

Four snap shots of the ensemble-averaged velocity field and the turbulence field during the runup phase in the strong bore case are shown in Figs. 8 and 9, respectively.

The runup phase follows the collapse of the bore front and the formation of water tongue and lasts until the maximum runup height is reached (Fig. 8(d)). During this phase, the momentum flux is primarily balanced by the gravity force and viscous force. The turbulence intensity is weakened as the TKE is diffused and dissipated. The TKE series in Fig. 9 shows the translating, spreading and diluting of the intense turbulence field resulting from the bore collapse.

Shortly after the runup phase begins, the effects of bore collapse on the ensemble-averaged velocity field quickly diminish and the velocity inside the water tongue is almost uniform in a vertical water column (Fig. 8(a)). As the water tongue moves landwards, the effects of bottom stress accumulate and the water particles close to the beach face travel noticeably more slowly than those near the free surface (Fig. 8(b)). On the other hand, because of longer exposure to bottom friction and gravity, fluid particles near the tip of runup tongue move at a slower speed than those in the rear of the water tongue. A typical illustration of the spatial variation of the velocity field can be found in Fig. 8(c). In the same figure, we also notice a vertical surface in the

vicinity of the tip of runup tongue. The combination of the sharp surface gradient and strong velocity variations results in an interesting local phenomenon, called 'mini-collapse'.

To examine the 'mini-collapse' more closely, in Fig. 10 we show the free surface profiles as well as the velocity field in a small region very close to the tip of the runup tongue ( $1.60 \leq x \leq 1.80$ ) at four time instants. As shown in Fig. 10(a) and (b), the tip of the water tongue has come to a stop, while the water body behind it is still pushing landwards. Water particles near the free surface travel at much faster speed than those near the beach face (Fig. 10(b)). This feature resembles a bore before collapsing at the still-water shoreline (Fig. 5). Although the height of the 'mini' bore is only in the order of magnitude of 1 cm, it behaves in the similar way as the original bore, i.e., it collapses (Fig. 10(c)), generates turbulence locally and forms a new runup water tongue (Fig. 10(d)). The similarity between Figs. 6 and 10 is striking. Since the reconstruction step of VOF method requires a  $3 \times 3$  stencil to resolve the normal direction of the surface, we recommend that any VOF-based model have at least 6 grids resolving the mini-bore height in order to study the mini-collapse phenomenon. In our case, there are more than 10 grids resolving the mini-bore height, so we are confident that the mini-collapse is not a numerical artifact. Furthermore, results for mini-collapse are repeatable with finer resolutions.

Two snapshots of the velocity field and turbulence field for the weak bore are shown in Figs. 11 and 12, respectively. The duration of the runup phase of the weak bore is only about 55% of that of the strong bore case. Consequently, the velocity variation in the  $y$ -direction (Fig. 11(a)) is not as prominent as that in the strong bore case. By the time the effects of gravity and bottom friction accumulate to a noticeable degree (Fig. 11(b)), the runup tip of water has stopped and the down-rush phase has already started.

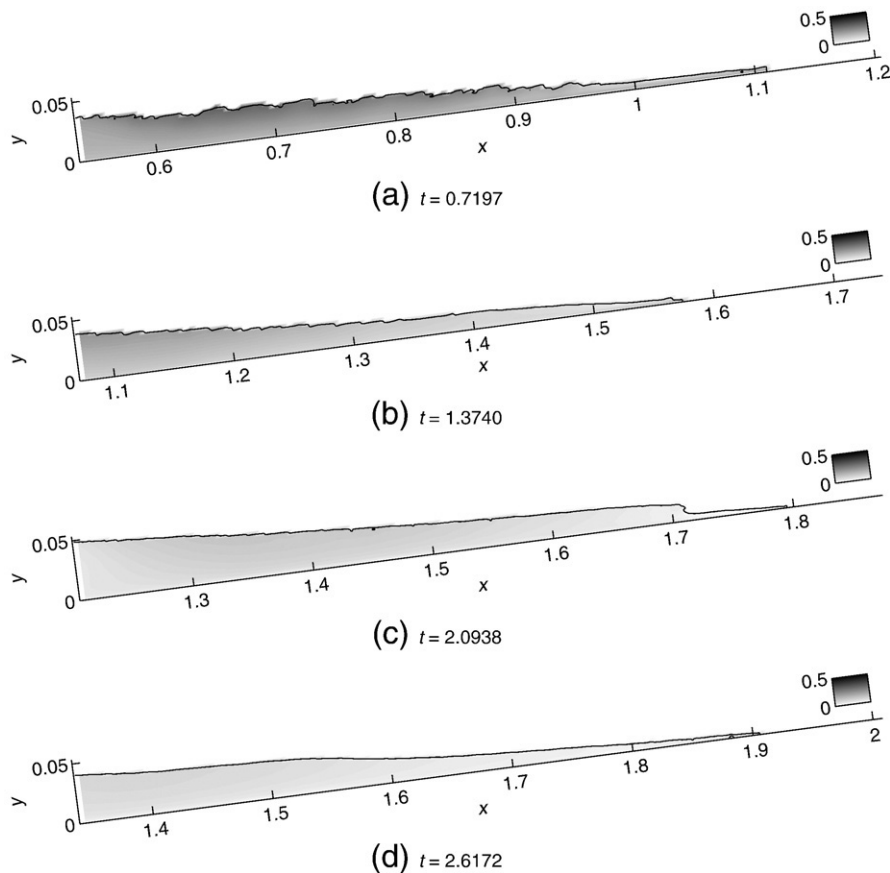


Fig. 9. Runup of the strong bore: turbulence intensity  $\sqrt{2k}$ .

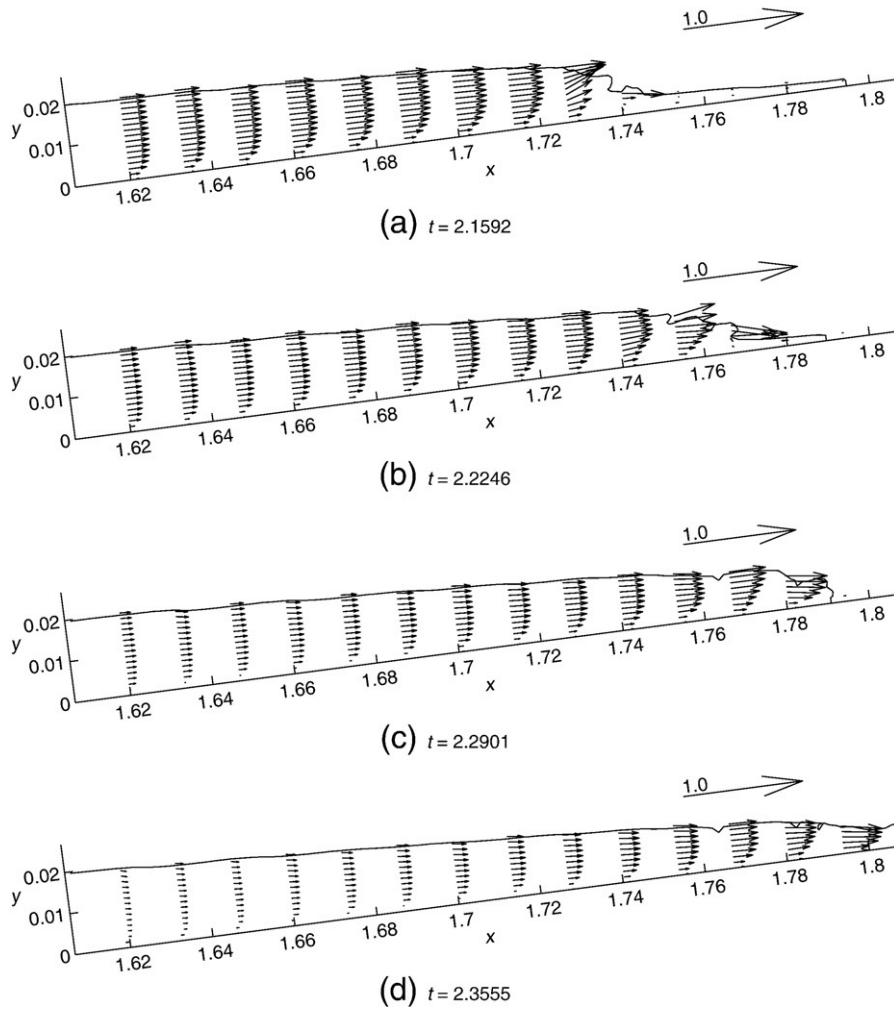


Fig. 10. Velocity field during a mini-collapse of the strong bore shown in Fig. 8.

Consequently, there is no obvious ‘mini-collapse’ during the runup phase of the weak bore.

4.3.2. Runup velocity

We show in Fig. 13 the numerical results for the time history of the bore position and shoreline locations. In the region of  $x < 0$ , the bore

position is defined as the toe of the bore, following the definition given in Yeh et al. (1989); in the region of  $x > 0$ , positions of the shoreline (tip of the runup tongue) are recorded after bore collapse. In both the strong and weak bore cases, the bore front slows down as it approaches the still-water shoreline ( $x=0$ ) and the bore collapse pushes shoreline to move with a faster speed. However, the shoreline

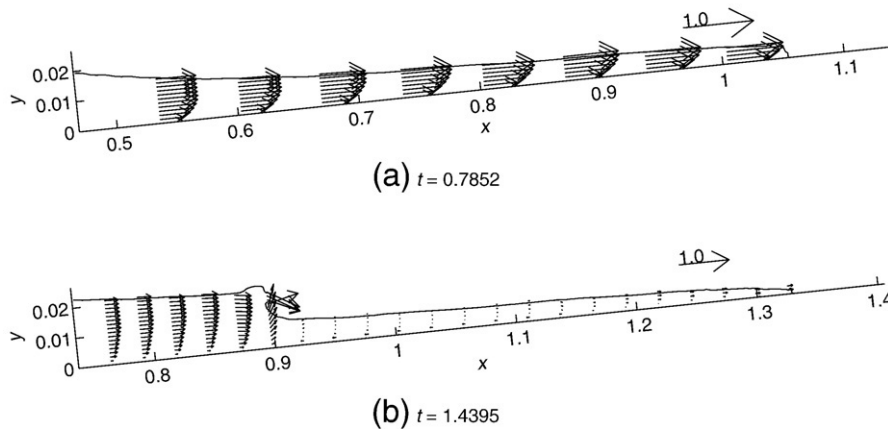


Fig. 11. Runup of the weak bore: non-dimensional mean velocity field  $\langle U \rangle$ .

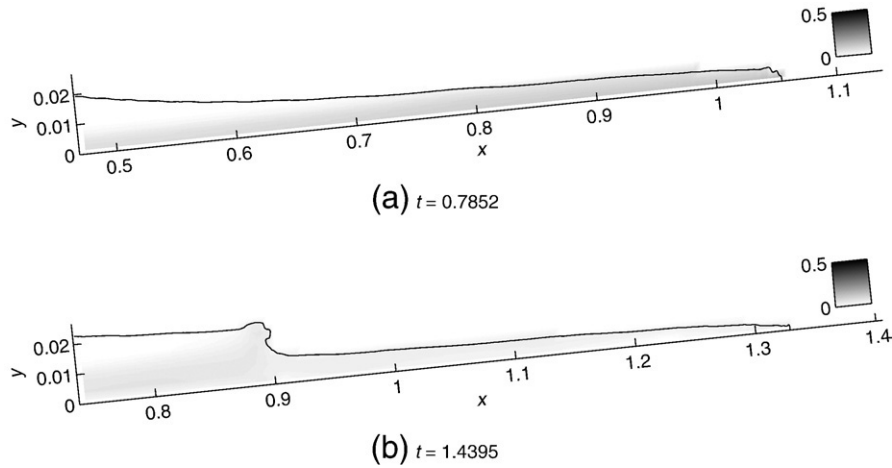


Fig. 12. Runup of the weak bore: turbulence intensity  $\sqrt{2k}$ .

movement is gradually slowed down by the gravity force and the bottom friction.

In Fig. 13, the mini-collapse in the strong bore case can be clearly identified at  $x=1.8$ , where the shoreline velocity becomes zero and then suddenly the shoreline moves landwards with a substantial velocity. On the other hand, in the weak bore case, no mini-collapse can be identified. Differentiating the location of the bore front and the shoreline with respect to time, we obtain the bore front velocities and shoreline runup velocities:

$$U_f(x, t) = \begin{cases} \frac{U_f \cos \beta}{U^*} & x \leq 0 \\ \frac{dx_b}{dt} & x > 0 \end{cases} \quad (20)$$

where  $x_b(t)$  marks the location of the runup tip.

In Fig. 14 numerical results of Eq. (20) are shown together with experimental data of Yeh et al. (1989), theoretical predictions (Whitham, 1958; Ho and Meyer, 1962), and previous numerical results by Hibberd and Peregrine (1979), based on the NSW theory.

From both Figs. 13 and 14, the present numerical results show that during the shoaling phase ( $-1 < x < 0$ ) the bore front velocity increases first and then slows down as the bore approaches the still-water shoreline. The smallest bore front velocities in experimental and the

present numerical results are in good agreement and are much smaller than those predicted by the NSW theory. After the bore collapse, the runup speed of the shoreline increases drastically within a short distance.

Both experimental data and the present numerical results indicate that the maximum runup velocities do not occur at the still-water shoreline, but at locations landward from it (i.e.,  $x=0.311$  in the strong bore case and  $x=0.108$  in the weak bore case). This is due to the fact that the actual bore collapse is a gradual transition. In the present numerical results, the maximum runup velocity after bore collapse is roughly the same as the maximum bore front velocity before bore collapse. Experimental results in the weak bore case confirms this. In the strong bore case, the bore toe location has very large uncertainties, both experimentally and numerically, due to the very fragmented free surface. Consequently, bore front velocity based on the differentiation of the time history of bore toe location has even larger uncertainties, which might explain the large deviation of our numerical results in  $x < -0.5$  in Fig. 14(a).

Again, the runup velocity clearly demonstrates the occurrence of a mini-collapse for the strong bore case. In Fig. 14, a small hump in the shoreline velocity near  $x=1.74$  can be identified, where the bore front velocity becomes almost zero. However, in a very short distance shoreward, the velocity jumps up and then decreases gradually to zero

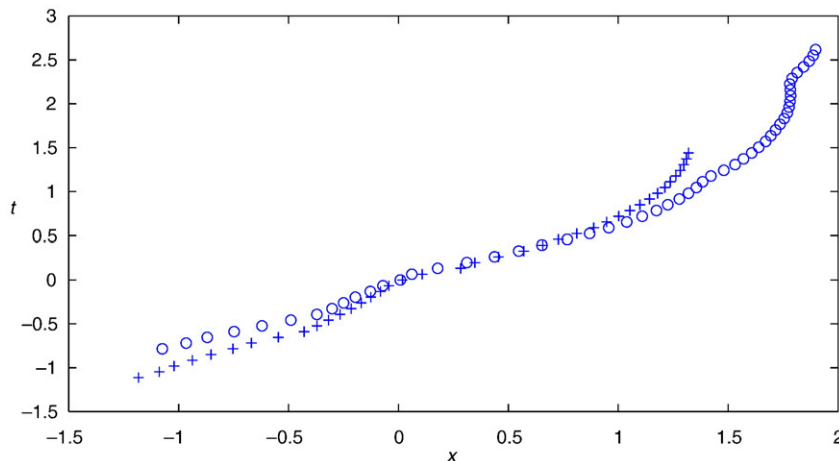
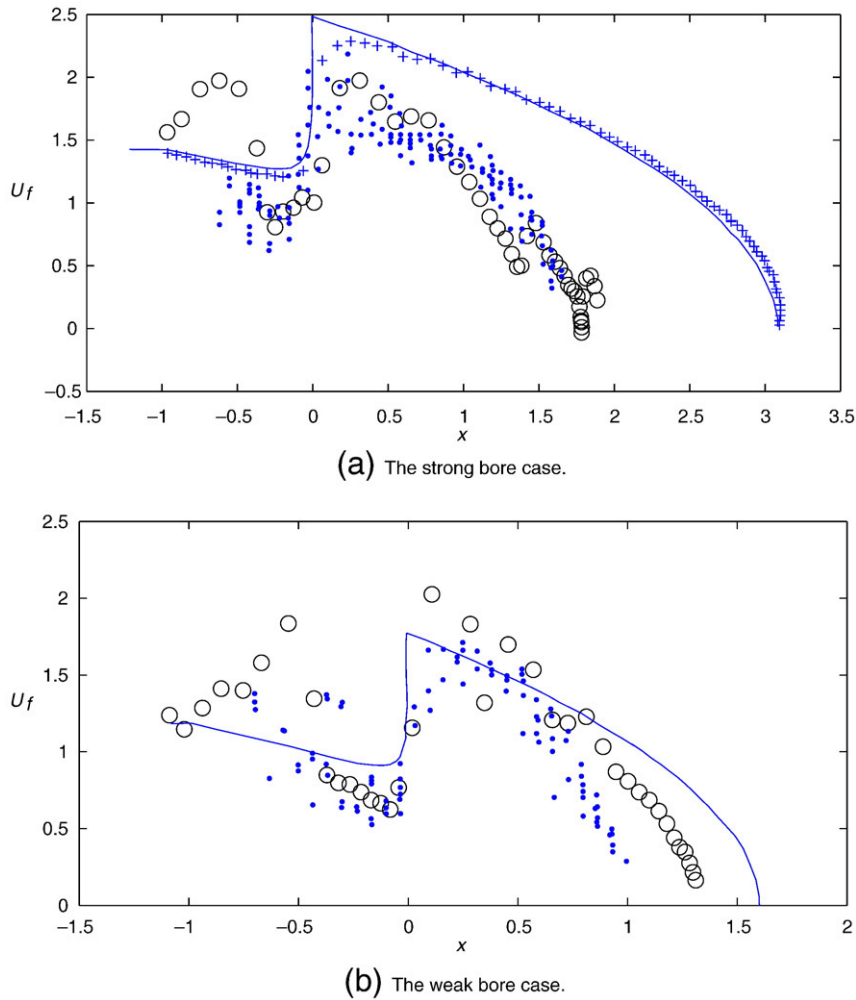


Fig. 13. Bore front and shoreline movement for the strong bore (O O) and the weak bore (+ +).  $x=-1$  marks the beach toe. The bore front position is defined by the bore toe location for  $x < 0$ . For  $x > 0$ , the shoreline position is defined as the rightmost location where the water depth is larger than  $2\Delta y$ .



**Fig. 14.** Bore front velocities and shoreline runup velocities. Solid lines represent theoretical results by Whitham (1958) and Ho and Meyer (1962); ++ numerical results by Hibberd and Peregrine (1979); ●● experimental results (including 6 repeated runs) by Yeh et al. (1989); ○○ present numerical results.

again. This implies that a small-scale free surface discontinuity has caught up with the tip of the water tongue, broken there and ran up again.

The experimental data for the bore front velocity contain large scattering with high uncertainties, particularly at the beginning of the runup phase where the turbulence intensity is high. However, as the bore front progresses, the influence of breaking becomes less significant and the dynamic process is mostly governed by the gravity and the viscous stresses. Accordingly, in Fig. 14, the scattering in experimental data becomes smaller and the present numerical results and experimental data agree with each other better at the end of the runup phase for the strong bore case. In the weak bore case the agreement is less satisfactory because of the over-prediction of the maximum runup velocity. The reason of this over-prediction is not clear yet at this point.

4.3.3. TKE evolution

To study the evolution of the TKE during the runup phase, we shall examine the depth-averaged TKE:

$$\bar{k}(x, t) = \frac{\int_0^{h+\eta} k(x, y, t) dy}{\int_0^{h+\eta} dy}, \tag{21}$$

where  $t$  is limited to  $t < T$  with  $T$  being the time at the end of runup phase.

We further define  $\bar{k}_m(x, t)$  as the maximum value of  $\bar{k}(x, t)$ , which occurs at  $t_m(x)$ . Finally, we also define the averaged TKE in the entire swash zone as

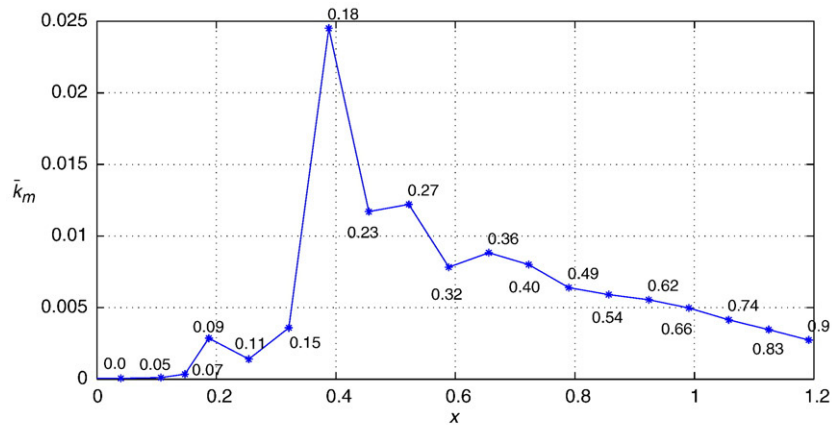
$$\bar{K}(t) = \frac{\int_0^{y_e} \int_0^{x_e} k(x, y, t) f(x, y, t) dx dy}{\int_0^{y_e} \int_0^{x_e} f(x, y, t) dx dy}, \tag{22}$$

where the color function

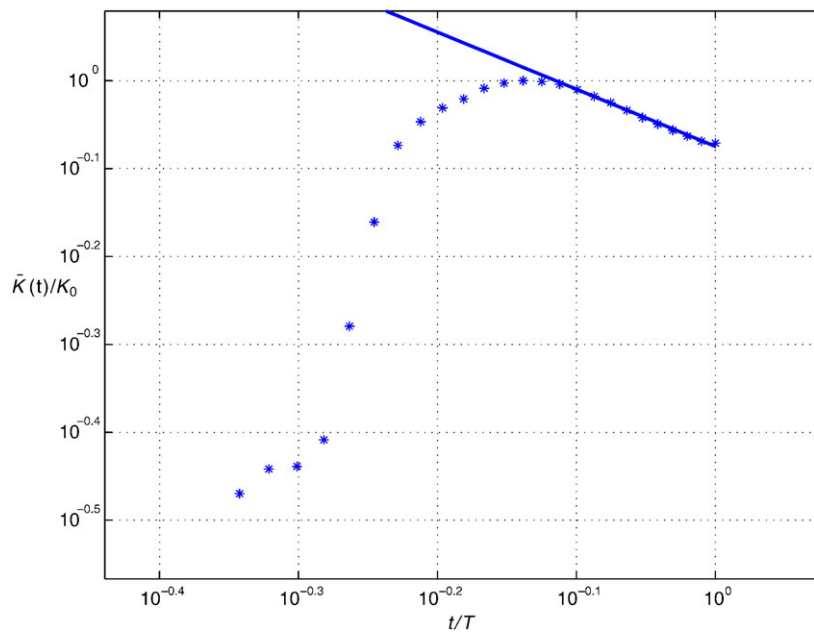
$$f(x, y, t) = \begin{cases} 0 & \text{no water} \\ 1 & \text{otherwise,} \end{cases}$$

and  $(x_e, y_e)$  are the end of computational domain in the  $x$ - $y$  coordinates.

In the weak bore case, the spatial distribution of  $\bar{k}_m(x, t)$  is shown in Fig. 15(a), while the decay of  $\bar{K}(t)/K_0$  with respect to  $t_m(x)/T$  is shown in Fig. 15(b). Note that  $K_0 = \max(\bar{K}(t))$  and  $T = 1.44$  is the end time of the runup phase. The maximum averaged TKE happens at the beginning of the runup phase, in which the dominant process is the dissipation of the TKE. Since  $t_m(x)$  increases monotonically in Fig. 15 (a), the advection process is also taking place. In addition, the TKE decay rate ( $-0.65$ ) is only half of that of the strong bore case (see Fig. 15). Sou (2006) reported that the TKE decay rate during the down-rush phase in her experiments is  $-1.0$ . This is comparable to the decay rate in the runup phase of the weak bore studied here, since bottom boundary layer generated turbulence dominates in both cases. However, the turbulence production during the runup phase is in general



(a) The maximum value of the cross-sectional averaged TKE,  $\bar{k}_m(x)$ .



(b) TKE decay with respect to time ( $T = 1.44$ ).

**Fig. 15.** TKE decay in the runup phase of the weak bore case. In (a) the numbers near ‘\*’ are  $t_m(x)$ . In (b) ‘\*’ represents numerical results while the solid lines is the power law with slope of  $-0.65$ .  $t = T$  marks the end of the runup phase.

larger than that in the down-rush phase because of larger frictional velocity and therefore turbulence should decay at a slower rate in the runup phase. This also implies that the present numerical results are qualitatively predicting a transient turbulent boundary layer.

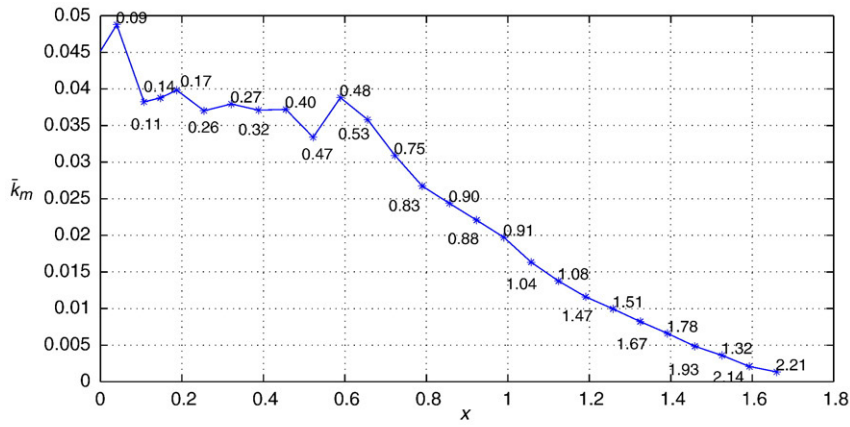
In the strong bore case, while  $\bar{k}_m(x,t)$  is shown in Fig. 16(a), the decay of  $\bar{k}(t)/K_0$  as a function of  $t_m(x)/T$  is shown in Fig. 16(b) where  $T=2.62$ .

The fact that  $\bar{k}_m(x,t)$  decreases monotonously along the slope implies that there is no strong TKE production after the collapse of the bore. However, there is a region ( $0.1 < x < 0.6$ ) where the dissipation of TKE is roughly balanced by the production of TKE. After that, the advection and dissipation of TKE dominate. From their experimental results, Petti and Longo (2001) made similar remarks: ‘Turbulent energy flux is essentially directed shoreward’.

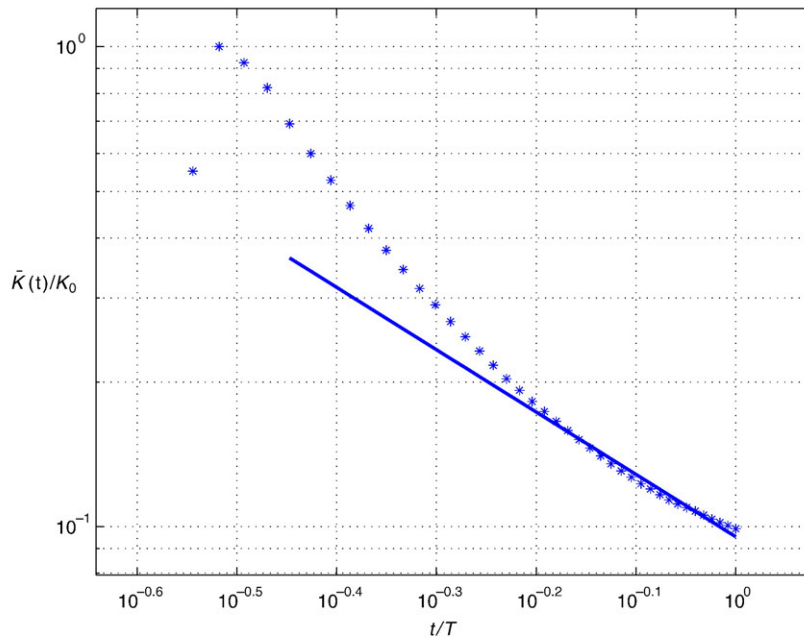
The first half of the runup phase ( $t \in [10^{-0.45}, 10^{-0.2}T]$ ) features a very strong TKE decay rate, which decreases monotonically in time so that in the second half of the runup phase ( $t \in [10^{-0.2}T, T]$ ) the TKE has a power-law decay with a  $-1.3$  slope, similar to that of the homo-

geneous grid turbulence. Spatially, this happens in the upper swash zone near the maximum runup. Interestingly, the experimental works of Cowen et al. (2003) also showed a grid turbulence decay rate even for a totally different setup (their experiments are for periodic waves propagating on a milder slope). This is, however, not unexpected. At the beginning of the runup phase, the effect of bore collapse still affect the turbulence field in terms of the produced anisotropy of Reynolds stresses. After a certain amount of time, this anisotropy dies out and the turbulence field becomes almost homogeneous; meanwhile the production of TKE diminishes and dissipation becomes the dominant process. Under these two conditions, the turbulence decay rate becomes similar to that of the grid turbulence.

We remark here that the  $k-\epsilon$  closure employed herein is one of many turbulence models based on the turbulent viscosity hypothesis (TVH), in which the *intrinsic assumption* is that Reynolds stress anisotropy is a function of mean velocity gradients ( $a_{ij}=f(\bar{S}_{ij})$ ) and the *specific assumption* specifies the form of the function, e.g., linear models assume  $a_{ij}=-2\nu_t \bar{S}_{ij}$ . This is a direct analogy to the viscous



(a) The maximum value of the cross-sectional averaged TKE,  $\bar{k}_m(x)$



(b) TKE decay with respect to time ( $T = 2.62$ ).

Fig. 16. TKE decay in the runup phase of the strong bore case. The caption is the same as that of Fig. 15 except that the slope of the solid line is  $-1.3$ .

stress–strain relation in a Newtonian fluid. As pointed out by Pope (2000), the molecular time-scale is relatively small so that the statistical state of molecular motions rapidly adjusts to the imposed straining, thus the justification of the intrinsic assumption. However, in turbulent flows with strong vorticity or large streamline curvature, the ratio of the turbulence time-scale  $k/\epsilon$  to the shear time-scale  $\bar{S}^{-1}$  is often very large, thus turbulence does not adjust rapidly to the imposed mean straining and the intrinsic assumption has no general basis. The present numerical results show that in the bore collapse phase  $\max(\bar{S}k/\epsilon) \approx 10^3$  and the averaged TKE near the still-water shoreline does not converge on grids with different resolutions. This suggests that we might need a better model (e.g., rapid distortion theory) than the TVH based turbulence model to capture the details during the bore collapse phase. However, in the runup phase, the time-scale of the mean strain is typically very small and the  $k-\epsilon$  model is applicable. Using different grid sizes, the decay rate of the averaged TKE in the strong bore case converges to the  $-1.3$  power law.

#### 4.4. Down-rush

During the down-rush phase the water tongue is pulled seawards by the gravity force and the seaward movements are resisted by bottom viscous stress. The free surface remains more or less horizontal during this phase.

Velocity field of the strong bore during the down-rush phase are shown in Fig. 17. At the beginning of the down-rush (Fig. 17(a)), the velocity is relatively small, but complex. The velocity profiles far away from the tip of the tongue are similar to those of a strong wall-jet. A very thin transient boundary layer is developing underneath the wall-jet-like flow. While most of water particles in the runup tongue have started moving seawards, the tip of the tongue is still running shoreward (see Figs. 17(a) and 18). As the gravity force pulls the runup tongue down the slope, the velocity profiles become more uniform in the water column. However, seaward velocity intensity varies along the slope. The depth-averaged velocities at the same four instants as shown in Fig. 17 are plotted in Fig. 18. It is clear that in the region

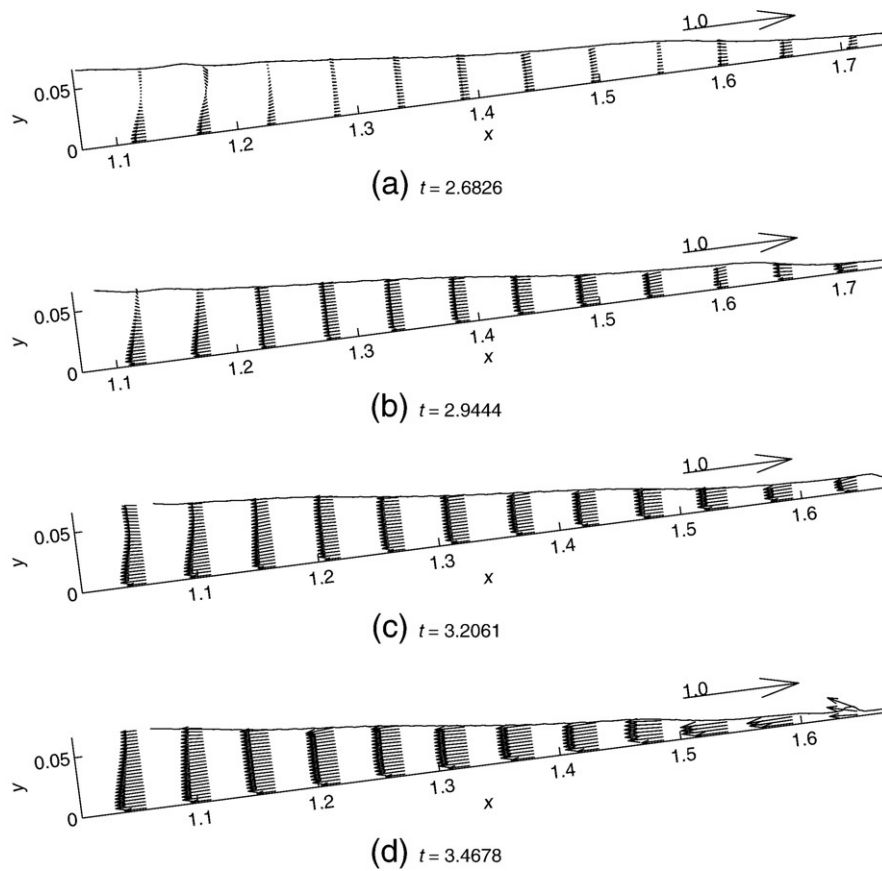


Fig. 17. Down-rush of the strong bore: non-dimensional mean velocity field  $\langle U \rangle$ .

$1.60 < x < 1.70$ , the down-rush velocity increases quickly in the seaward direction, while the water depth also increase substantially within a short distance (see Fig. 17). The free surface forms a bore-like feature, which is almost stationary before being washed away. This phenomenon is very similar to the ‘back-wash bore’ discussed by Hibberd and Peregrine (1979) in their numerical solutions of NSW equations. The turbulence level in the down-rush phase is much lower than that in the runup phase.

Four snapshots of the down-rush phase in the weak bore case are shown in Fig. 19 for velocity and in Fig. 20 for vorticity. The free surfaces tilt landward in these plots due to a scaling of the  $y$ -axis; in reality the free surface should tilt seaward. The corresponding depth-averaged on-offshore velocities are also shown in Fig. 21. A surface signature similar to the ‘back-wash bore’ is also observed in Fig. 19. As shown in Fig. 19(a), as the tip of runup tongue has already started to move seaward the rest of bore is still propagating shoreward. These two opposite currents interact violently with each other, generating strong vorticity at the location of the ‘back-wash bore’, as shown in Fig. 20. This feature has also been observed by Sou (2006) in her experiments. On the seaward side of the bore, the velocity profiles show strong variations in all directions. Fig. 21 indicates that the depth-averaged velocities are in the opposite directions across the ‘back-wash bore’ in the weak bore case and the intensity of the bore is much stronger than that in the strong bore case.

5. Conclusions

Based on the numerical results shown in this paper, as well as previous experimental observations, the process of bore propagation over a slope can be described as follows. The bore height remains roughly constant during the shoaling phase. While the weak bore does not break, the strong bore breaks as a plunger before it reaches the still-water shoreline. As the strong bore approaches the still-water shoreline, the water wedge in front of the bore is pushed up by the bore and serves as a buffer to slow down the bore. In both cases, the height of the bore does not go to zero suddenly at the shoreline. Although the bore collapse lasts a short period of time, it is still gradual and is best viewed as the adaptation of the bore to the slope.

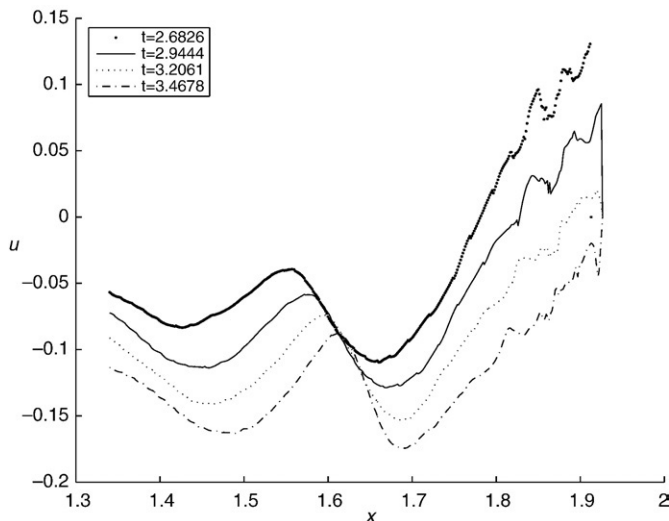


Fig. 18. The depth-averaged velocity for the strong bore at four time instants.

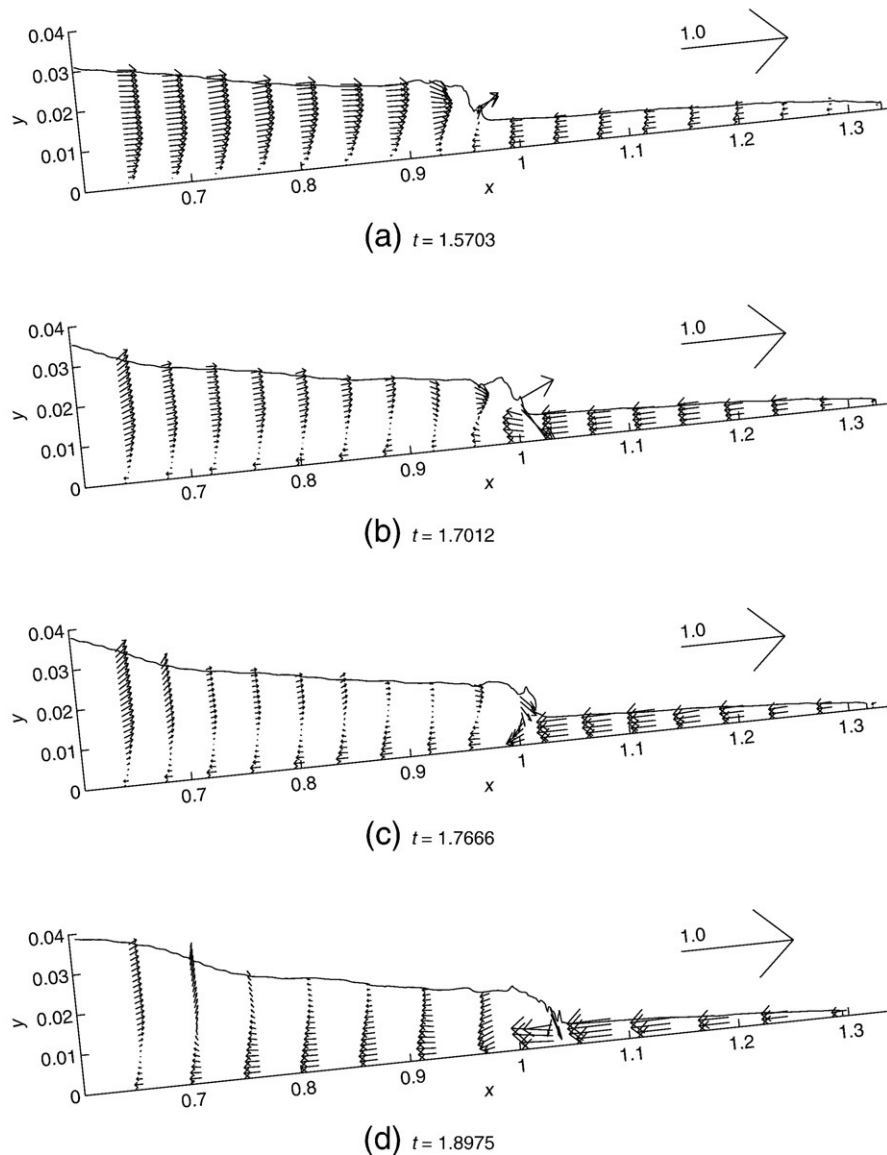


Fig. 19. Down-rush of the weak bore: non-dimensional mean velocity field  $\langle U \rangle$ .

During the bore collapse, the bore front velocity first slows down and then speeds up. In the runup and the down-rush phase, in addition to the gravity force, the bottom stress also plays an important role. The spatial gradients in the vertical direction and the on-offshore direction eventually lead to the occurrence of two small-scale processes: 'mini-collapse' and 'back-wash bore', the former remarkably resembles bore collapse qualitatively.

As for the turbulence field in the strong bore case, the present numerical results show that the TKE are confined in the frontal zone of the bore before it collapses. Bore collapse produces high TKE and the maximum turbulence intensity occurs at the still-water shoreline. In the runup phase, the TKE produced by bore collapse is advected, diffused and dissipated. There are two distinct phases with respect to turbulence decay rate: in the lower swash zone near the still-water shoreline, effects of the bore collapse on the turbulence field persist, while in the upper swash zone near the maximum runup, the turbulence becomes almost homogeneous and decays like the grid turbulence does. In contrast, the turbulence evolution in the weak bore case does not have the first phase and the power-law decay of the

TKE starts at the beginning of the runup phase. In addition, the maximum TKE occurs at a location landward of the still-water shoreline and the decay rate is only about half of that in the strong bore case.

#### Acknowledgements

This research has been supported by grants from the National Science Foundation (Fluid Dynamics Program, Physical Oceanography Program and ITR program) and from the Office of Naval Research (Geoscience Program) to Cornell University. We would also like to thank Dr. Harry Yeh for providing the pictures shown in the paper.

#### References

- Amoudry, L., Hsu, T.J., Liu, P.L.F., 2008. Two-phase model for sand transport in sheet flow regime. *J. Geophys. Res.* 113, c03011. doi:10.1029/2007JC004179.
- Baldock, T.E., Hughes, M.G., 2006. Field observations of instantaneous water slopes and horizontal pressure gradients in the swash-zone. *Cont. Shelf Res.* 26 (5), 574–588 Apr.

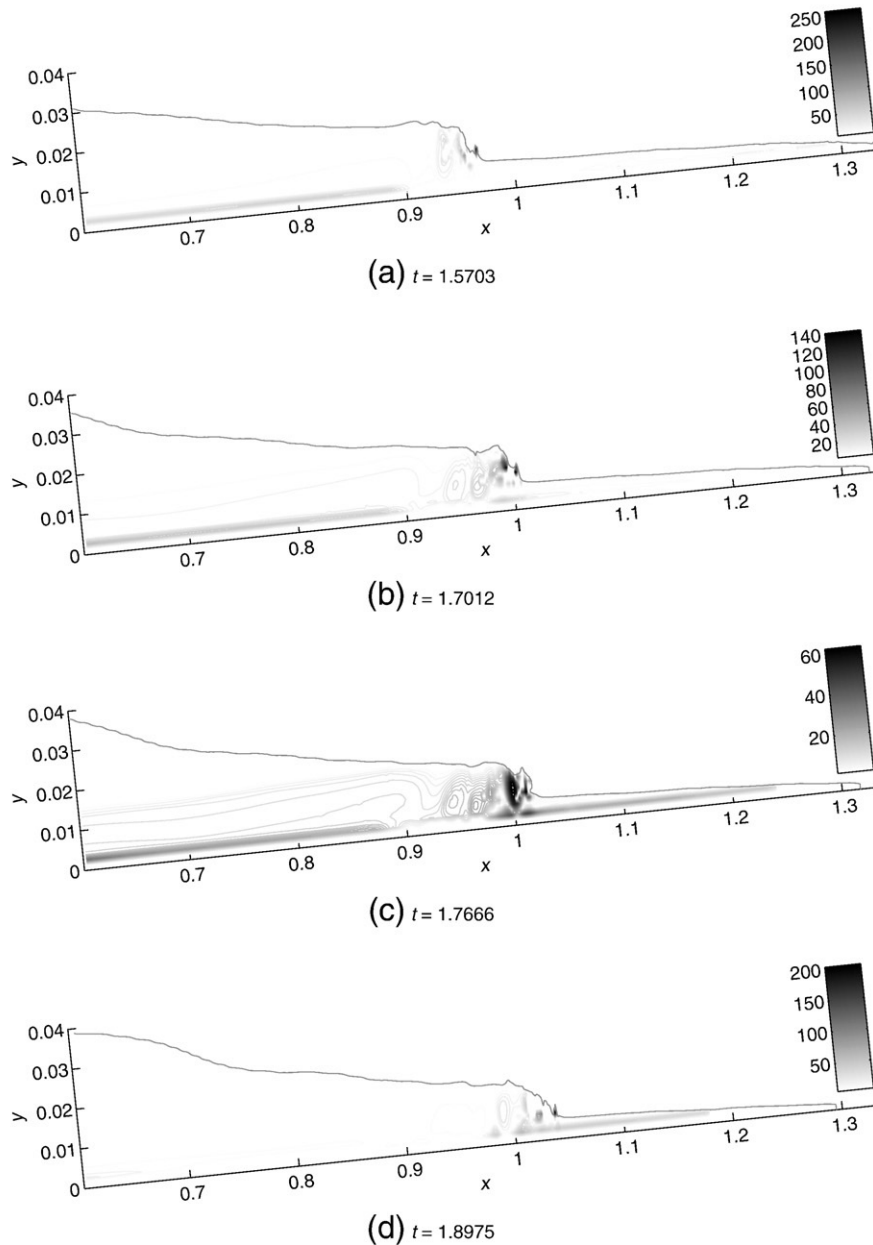


Fig. 20. Down-rush of the weak bore: vorticity normalized by  $1/T^*$ .

- Baldock, T.E., Hughes, M.G., Day, K., Louys, J., 2005. Swash overtopping and sediment overwash on a truncated beach. *Coast. Eng.* 52 (7), 633–645.
- Brackbill, J.U., Kothe, D.B., Zemach, C., 1992. A continuum method for modeling surface tension. *J. Comput. Phys.* 100 (2), 335–354.
- Chorin, A.J., 1968. Numerical solution of the Navier–Stokes equations. *Math. Comput.* 22 (104), 745–762 Oct.
- Chorin, A.J., 1969. On the convergence of discrete approximations to the Navier–Stokes equations. *Math. Comput.* 23 (106), 341–353 Apr.
- Cowen, E.A., Sou, I.M., Liu, P.L.F., Raubenheimer, B., 2003. Particle image velocimetry measurements within a laboratory-generated swash zone. *J. Eng. Mech.* 129 (10), 1119–1129.
- Drake, T.G., Calantoni, J., 2001. Discrete particle model for sheet flow sediment transport in the nearshore. *J. Geophys. Res.* 106, 19859–19868.
- Elfrink, B., Baldock, T.E., 2002. Hydrodynamics and sediment transport in the swash zone: a review and perspectives. *Coast. Eng.* 45 (3–4), 149–167.
- Garcia, N., Lara, J.L., Losada, I.J., 2004. 2-d numerical analysis of near-field flow at low-crested permeable breakwaters. *Coast. Eng.* 51 (10), 991–1020.
- Guard, P.A., Baldock, T.E., 2007. The influence of seaward boundary conditions on swash zone hydrodynamics. *Coastal Eng.* 54, 321–331.
- Hibberd, S., Peregrine, D.H., 1979. Surf and run-up on a beach: a uniform bore. *J. Fluid Mech.* 95, 323–345 Nov.
- Hirt, C.W., Nichols, B.D., 1981. Volume of fluid (VOF) method for the dynamics of free boundaries. *J. Comput. Phys.* 39 (1), 201–225.
- Ho, D.V., Meyer, R.E., 1962. Climb of a bore on a beach. Part 1. Uniform beach slope. *J. Fluid Mech.* 14 (2), 305–318.
- Horn, D.P., 2006. Measurements and modelling of beach groundwater flow in the swash-zone: a review. *Cont. Shelf Res.* 26 (5), 622–652 Apr.
- Hsu, T.J., Liu, P.L.F., 2004. Toward modeling turbulent suspension of sand in the nearshore. *J. Geophys. Res.* 109, C06018.
- Hsu, T.J., Raubenheimer, B., 2006. A numerical and field study on inner-surf and swash sediment transport. *Cont. Shelf Res.* 26 (5), 589–598 Apr.
- Hsu, T.J., Jenkins, J.T., Liu, P.L.F., 2003. On two-phase sediment transport: dilute flow. *J. Geophys. Res.* 108 (C3), 3057–3070.
- Hsu, T.J., Sakakiyama, T., Liu, P.L.F., 2002. A numerical model for wave motions and turbulence flows in front of a composite breakwater. *Coast. Eng.* 46 (1), 25–50.
- Hughes, M.G., Baldock, T.E., 2004. Eulerian flow velocities in the swash zone: field data and model predictions. *J. Geophys. Res.* 109 (C08009).
- Jensen, A., Pedersen, G.K., Wood, D.J., 2003. An experimental study of wave run-up at a steep beach. *J. Fluid Mech.* 486, 161–188.
- Jones, W.P., Launder, B.E., 1972. Prediction of laminarization with a two-equation model of turbulence. *Int. J. Heat Mass Transfer* 15 (2), 301–314.
- Kothe, D.B., Mjolsness, R.C., 1992. Ripple: A new model for incompressible flows with free surfaces. *AIAA J.* 30 (11), 2694–2700.
- Lara, J.L., Garcia, N., Losada, I.J., 2006. RANS modelling applied to random wave interaction with submerged permeable structures. *Coast. Eng.* 53 (5–6), 395–417.

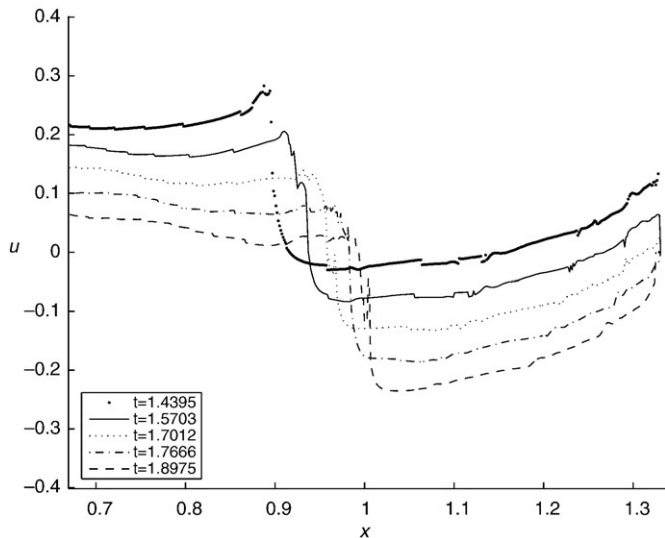


Fig. 21. Depth-averaged velocity for the weak bore at four time instants.

- Larson, M., Erikson, L., Hanson, H., 2004. An analytical model to predict dune erosion due to wave impact. *Coast. Eng.* 51 (8–9), 675–696.
- Lauder, B.E., Sharma, B.L., 1974. Application of the energy-dissipation model or turbulence to the calculation of flow near a spinning disc. *Lett. Heat Mass Transf.* 1 (2), 131–138 November.
- Lax, P., Wendroff, B., 1960. Systems of conservation laws. *Comm. Pure Appl. Math.* 13, 217–237.
- Lemos, C.M., 1992. Wave Breaking: a Numerical Study, Volume 71 of Lecture Notes in Engineering. Springer-Verlag, Berlin; New York 0387549420.
- Leveque, R.J., Li, Z., 1994. Immersed interface method for elliptic equations with discontinuous coefficients and singular sources. *SIAM J. Numer. Anal.* 31 (4), 1019–1044.
- Li, Z., Lai, M.C., 2001. The immersed interface method for the Navier–Stokes equations with singular forces. *J. Comput. Phys.* 171 (2), 822–842.
- Lin, P. Numerical modeling of breaking waves. PhD thesis, Cornell University, Aug. 1998.
- Lin, P., Liu, P.L.F., 1998a. Numerical study of breaking waves in the surf zone. *J. Fluid Mech.* 359, 239–264.
- Lin, P., Liu, P.L.F., 1998b. Turbulence transport, vorticity dynamics, and solute mixing under plunging breaking waves in surf zone. *J. Geophys. Res.* 103 (C8), 15677–15694.
- Lin, P., Chang, K.A., Liu, P.L.F., 1999. Runup and rundown of solitary waves on sloping beaches. *J. Waterw. Port Coast. Ocean Eng.* 125 (5), 247–255.
- Liu, P.L.F., Al-Banaa, K., 2004. Solitary wave runup and force on a vertical barrier. *J. Fluid Mech.* 505 (505), 225–233.
- Liu, P.L.F., Lin, P., Chang, K.A., Sakakiyama, T., 1999. Numerical modeling of wave interaction with porous structures. *J. Waterw. Port Coast. Ocean Eng.* 125 (6), 322–330.
- Liu, P.L.F., Lynett, P., Synolakis, C.E., 2003. Analytical solutions for forced long waves on a sloping beach. *J. Fluid Mech.* 478 (478), 101–109.
- Liu, P.L.F., Wu, T.R., Raichlen, F., Synolakis, C.E., Borrero, J.C., 2005. Runup and rundown generated by three-dimensional sliding masses. *J. Fluid Mech.* 536, 107–144.
- Madsen, P.A., Svendsen, I.A., 1983. Turbulent bores and hydraulic jumps. *J. Fluid Mech.* 129, 1–25 April.
- Masselink, G., Puleo, J.A., 2006. Swash-zone morphodynamics. *Cont. Shelf Res.* 26 (5), 661–680 Apr.
- Masselink, G., Russell, P., 2006. Flow velocities, sediment transport and morphological change in the swash zone of two contrasting beaches. *Mar. Geol.* 227 (3–4), 227–240.
- Miller, R.L., 1968. Experimental determination of run-up of undular and fully developed bores. *J. Geophys. Res.* 73 (14), 4497–4510.
- Nielsen, P., 2002. Shear stress and sediment transport calculations for swash zone modeling. *Coast. Eng.* 45, 53–60.
- Packwood, A.R., Surf and run-up on beaches. PhD thesis, Bristol University, 1980.
- Peregrine, D.H., 1983. Breaking waves on beaches. *Annu. Rev. Fluid Mech.* 15, 149–178.
- Peregrine, D.H., Williams, S.M., 2001. Swash overtopping a truncated plane beach. *J. Fluid Mech.* 440 (440), 391–399.
- Peskin, C.S., 1972. Flow patterns around heart valves: a numerical method. *J. Comput. Phys.* 10, 252–271.
- Peskin, C.S., 1977. Numerical analysis of blood flow in the heart. *J. Comput. Phys.* 25, 220–252.
- Petti, M., Longo, S., 2001. Turbulence experiments in the swash zone. *Coast. Eng.* 43 (1), 1–24.
- Pope, S.B., 2000. Turbulent flows. Cambridge University Press, Cambridge; New York. . 0521591252; 0521598869.
- Puleo, J.A., 2003. Fluid acceleration effects on suspended sediment transport in the swash zone. *J. Geophys. Res.* 108 (C11), 3350. doi:10.1029/2003JC001943.
- Puleo, J.A., Farhadzadeh, A., Kobayashi, N., 2007. Numerical simulation of swash zone fluid accelerations. *J. Geophys. Res.* 112, C07007. doi:10.1029/2006JC004084.
- Raubenheimer, B., 2002. Observations and predictions of fluid velocities in the surf and swash zones. *J. Geophys. Res.* 107 (C11), 3190 Nov.
- Rodi, W., 1980. Turbulence Models and Their Application in Hydraulics: a State of the Art Review. International Association for Hydraulic Research, Delft, The Netherlands. 9021270021.
- Sallenger, A.H., Krabill, W., Brock, J., Swift, R., Manizade, S., Stockdon, H., 2002. Sea-cliff erosion as a function of beach changes and extreme wave runup during the 1997–1998 El Nino. *Mar. Geol.* 187 (3–4), 279–297.
- Shen, M.C., Meyer, R.E., 1963a. Climb of a bore on a beach part 3. Run-up. *J. Fluid Mech.* 16 (1), 113–125.
- Shen, M.C., Meyer, R.E., 1963b. Climb of a bore on a beach part 2. Non-uniform beach slope. *J. Fluid Mech.* 16 (1), 108–112.
- Shigematsu, T., -F Liu, P.L., Oda, K., 2004. Modelisation numerique des etapes initiales de l'onde de rupture de barrage; numerical modeling of the initial stages of dam-break waves. *J. Hydraul. Res.* 42 (2), 183–195.
- Shin, S., Cox, D., 2006. Laboratory observations of inner surf and swash-zone hydrodynamics on a steep slope. *Cont. Shelf Res.* 26 (5), 561–573 Apr.
- Shih, T.H., Zhu, J., Lumley, J.L., 1996. Calculation of wall-bounded complex flows and free shear flows. *Int. J. Numer. Meth. Fluids* 23 (11), 1133–1144 Dec.
- Sou, I.M. An experimental investigation of the turbulence structure within the surf and swash zones. PhD thesis, Cornell University, Jan. 2006.
- Stoker, J.J., 1957. *Water Waves: the Mathematical Theory with Applications*. Wiley, New York 0471570346.
- Sturtevant, B., 1965. Implications of experiments on weak undular bore. *Phys. Fluids* 8 (6), 1052–1055.
- Svendsen, I.A., Madsen, P.A., 1984. A turbulent bore on a beach. *J. Fluid Mech.* 148, 73–96 November.
- Turner, I.L., 1998. Monitoring groundwater dynamics in the littoral zone at seasonal, storm, tide and swash frequencies. *Coast. Eng.* 35 (1–2), 1–16.
- Turner, I.L., Nielsen, P., 1997. Rapid water table fluctuations within the beach face: implications for swash zone sediment mobility? *Coast. Eng.* 32 (1), 45–59.
- Whitham, G.B., 1958. On the propagation of shock waves through regions of non-uniform area or flow. *J. Fluid Mech.* 4, 337–360.
- Yeh, H.H., Ghazali, A., 1988. On bore collapse. *J. Geophys. Res.* 93 (C6), 6930–6936.
- Yeh, H.H., Ghazali, A., Marton, I., 1989. Experimental study of bore run-up. *J. Fluid Mech.* 206, 563–578.